BRILLOUIN SCATTERING EXPERIMENTS NEAR THE α-β PHASE TRANSITION IN SINGLE CRYSTALS OF N_2 AND CO

VAHID ASKARPOUR

BRILLOUIN SCATTERING EXPERIMENTS NEAR THE α-β PHASE TRANSITION IN SINGLE CRYSTALS OF N_2 AND CO

by

© Vahid Askarpour, B.Sc. (Hons.)

A Thesis submitted in partial fulfillment
of the requirements for the degree of
Master of Science

Department of Physics
Memorial University of Newfoundland

November 1986

St. John's Newfoundland

ISBN 0-315-36965-5

ABSTRACT

The technique of high resolution Brillouin spectroscopy has been used to determine the adiabatic elastic constants of large cooled single crystals of β-N_2 and β-CO in an effort to gain insight into the α-β phase transition of these two unique examples of diatomic molecules which are extremely similar in many physical and chemical properties. The crystals were grown in a quartz cell inside a liquid helium cryostat. Laue x-ray diffraction analysis provided for the determination of the orientations of these crystals relative to the laboratory frame of reference. An argon ion laser beam was incident on the crystal and the scattered beam was analysed at 90° relative to the incident beam by a piezo-electrically scanned triple-pass Fabry-Perot interferometer. The signals were then collected by a photomultiplier tube, amplified through an amplifier/discriminator assembly and finally recorded by the data acquisition and stabilization system.

The values of elastic constants of β-N_2 at 47.5 K in units of 10^9 N/m^2 (subject to an absolute uncertainty of about 2%) are: c_{11}=2.307 c_{12}=1.454 c_{13}=1.274 c_{33}=2.488 c_{44}=0.378

The values of elastic constants of β-CO at 62 K in units of 10^9 N/m^2 (subject to an absolute uncertainty of about 4%) are: c_{11}=2.013 c_{12}=1.212 c_{13}=0.998 c_{33}=2.227 c_{44}=0.402

These values were compared to those at the corresponding triple points. There is an approximate elastic constant increase of 1% per 1 K of temperature decrease and there seems to be no evidence for mode softening in either N_2 or CO.

Three large single crystals of β-CO were cooled slowly through the

phase transition resulting in three single crystals of α-CO. The orientations of these face centered cubic crystals were determined and correlated to those of the hexagonal close packed phase. It was noted that the hexagonal basal planes appear to prefer to transform to planes of the form {110} of the cubic structure. A possible mechanism is discussed and the result is compared to previous works on metals and molecular crystals that undergo h.c.p. to f.c.c. phase transition.

ACKNOWLEDGEMENTS

I wish to express my sincere appreciation and gratitude to my supervisors Dr. H. Kiefte and Dr. M. J. Clouter. Dr. Kiefte's help, guidance and encouragement played an invaluable, inspiring and vital role throughout this project and in the preparation of this thesis.

I am grateful to Mr. T. White and his staff for a steady supply of liquid Helium throughout the experiment and to Mr. R. Bradley for taking the photographs. Finally I would like to thank my friends for their helpful discussions and criticisms.

Throughout this research, I was supported by a Fellowship from Memorial University of Newfoundland which I gratefully acknowledge.

TABLE OF CONTENTS

LIST OF TABLES

LIST OF FIGURES

CHAPTER 1

INTRODUCTION

Brillouin spectroscopy is a very effective technique for probing the dynamical behavior of phonons in crystals and consequent lattice instability associated with phase transitions. In particular, it allows for accurate determination of elastic constants in single crystals. The present work constitutes an attempt to use Brillouin spectroscopy to study very simple phase transitions in diatomic molecular solids, i.e. solid N_2 and CO.

The α and β phases of solid N_2 and CO represent systems that undergo orientationally disordered hexagonal close-packed (h.c.p.) to orientationally ordered face centered cubic (f.c.c.) phase transitions. A knowledge of elastic constants is important in the sense that certain elastic constants may decrease in magnitude as the transition temperature is approached. This softening of certain elastic constants is caused by soft acoustic phonons travelling in the crystal (1). As a phase transition temperature is reached, the mechanical instability increases and certain lattice vibrational modes undergo a considerable energy decrease such that as their frequency decreases the interatomic binding forces are decreased. Eventually, the anharmonicity and vibration amplitudes are so large that atoms adopt new sites.

CO while chemically distinct, is physically very similar to N_2. The molecules are isoelectronic and have the same size and identical masses (see Table 1.1). Melting and boiling points are very similar and

TABLE 1.1

Some physical properties of N_2 and CO

	N_2		CO	
Molecular Weight	28.01	(A)	28.01	(A)
Atomic Number	14	(A)	14	(A)
Boiling Point	77.2 K	(A)	81.5 K	(A)
Triple Point Temperature	63.15 K	(C)	68.15 K	(B)
α-β Transition Temperature	35.6 K	(C)	61.55 K	(B)
Equilibrium Vapor Pressure				
At the Triple Point	93.905 mm Hg	(D)	115 mm Hg	(B)
Lattice Parameters				
Of the β Phase	a=0.405 nm		a=0.414 nm	
	c=0.6604 nm	(E)	c=0.685 nm	(F)
	c/a=1.63		c/a=1.65	
Lattide Parameter				
of the α Phase at 20 K	a=0.565 nm	(G)	a=0.565 nm	(G)

(A) See reference (2)

(B) See reference (3)

(C) See reference (4)

(D) See reference (5)

(E) See reference (6)

(F) See reference (7)

(G) See reference (8)

TABLE 1.1 continued

Elastic Constants at the Triple Point (in units of $10^9 N/m^2$)	c_{11}=1.825		c_{11}=1.901	
	c_{12}=1.131		c_{12}=1.146	
	c_{13}=0.98	(H)	c_{13}=0.951	(I)
	c_{33}=1.976		c_{33}=2.905	
	c_{44}=0.32		c_{44}=0.356	
Quadrupole Moment (in units of 10^{-26} esu.cm^2)	-1.51	(G)	-2.5	(G)
Dipole Moment (in units of 10^{-19} esu.cm)	0	(G)	1.12	(G)
Nuclear Separation	0.11 nm	(G)	0.11 nm	(G)

(H) See reference (9)

(I) See reference (10)

(G) See reference (8)

nearest neighbor distances and lattice constants are almost identical. There is a small dipole moment in CO due to its heteronuclear structure. A study of temperature dependence of molar volume (11) shows that CO and N_2 behave similarly above 70 K and below 20 K. Between these temperatures, N_2 like CO solidifies in a high temperature h.c.p. β phase and a low temperature f.c.c. α phase. The biggest dissimilarity between N_2 and CO is the α-β phase transition temperature. N_2 stays hexagonal from 63.15 K to 35.6 K whereas for CO, this range is from 68.15 K to 61.55 K. There are various possible reasons for this, one being that the quadrupole moment of CO is greater than N_2 and hence the associated interaction causes CO to orientationally order more readily (12), the other being that rotation-translation coupling is stronger for CO because of physical asymmetry, hence causing lattice instability to occur sooner than in N_2 (6). The following work determines the elastic constants of N_2 at 47.5 K, the elastic constants of CO at the triple point and at 62 K and correlates the orientations of the α and β phases of solid CO.

1-1 Structure And Phase Diagrams Of N_2 and CO

a)N_2

Solid N_2 exists in at least six crystal forms: ordered cubic α-N_2 (space group Pa3), disordered hexagonal β-N_2 (space group $P6_3/mmc$) ordered tetragonal γ-N_2 (space group $P4_2/mnm$), disordered cubic δ-N_2 (space group Pm3n), ε-N_2 probably rhombohedral (space group R$\bar{3}$c) and ζ-N_2 probably rhombohedral (space group R3c). Fig.1.1 shows the phase diagram of N_2 (13).

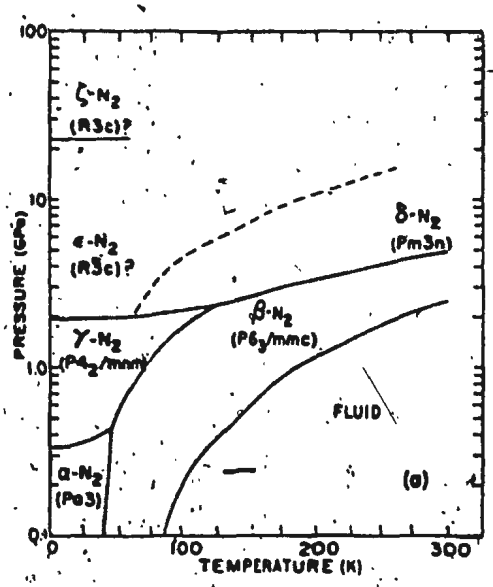

Fig.1.1 Phase diagram of Nitrogen.

An extensive review paper on condensed N_2 by Scott is available (4). Single crystals of β-N_2 of excellent quality can be grown by slow solidification at the triple point (4). Handling such a single crystal is difficult (as will be explained in section 2-7). Streib *et al.* (14) however, performed x-ray diffraction studies of a single crystal rather than powder samples (as was done by most researchers). They determined the structure and confirmed the molecular precession about the c-axis at 54.5° angle. Mills *et al.* (15) working on single crystals of N_2 at 2.94 GPa and 300 K confirmed the hexagonal structure of space group $P6_3/mmc$ using x-ray diffraction (see also x-ray intensity measurements by Bolz *et al.* (16)). Gannon and Morrison (17) studied the optical birefringence in β-N_2. They also confirmed the structure of β-N_2 to be

hexagonal $P6_3/mmc$. Klein *et al.* (18) theoretically calculated the dynamic structure factor $S(Q,\omega)$ of β-N_2. Elastic and inelastic neutron scattering have been carried out by Powell *et al.* (19) on single crystals of β-N_2 at 400 MPa and 55 K. They determined the elastic constants of β-N_2 at that temperature from slopes of dispersion curves. Kjems and Dolling (20) determined the elastic constants at 37 K and 0 Pa using the same technique. Kiefte and Clouter (9) accurately determined the elastic constants of single crystals of β-N_2 at 63 K using Brillouin spectroscopy. Theoretical calculation of elastic constants using self-consistent phonon approximation were carried out by Goldman and Klein (21).

Electron diffraction patterns of annealed tiny single crystallites in films of α-N_2 obtained by Venables and English (22) showed that the structure is cubic Pa3. Hurl and Morton (23) studied thin films of solid α-N_2 at 4 and 20 K using electron transmission diffraction and obtained the same result. X-ray intensity measurements by Bolz *et al.* (16) confirmed that the structure is Pa3. The structure is face centered cubic with a basis of four molecules per unit cell. The molecules are ordered in the basis such that the molecule is aligned parallel to <111> direction of cube.

Large single crystals of α-N_2 are extremely difficult to produce due to the highly disruptive nature of the α-β transition (as observed by Gannon and Morrison in the birefringence study of α-N_2 (17) and the consequent shattering of solid N_2). However (by chance), one single crystal of α-N_2 has been produced by Streib *et al.* (14) and by Kjems and Dolling (24). Venables (25) has grown a single crystal segment of α phase in a very thin film and studied it by electron microscopy. Other

studies include Raman spectroscopy of the α and γ phases at 4.2 K and pressure up to 0.9 GPa and spectroscopic observation of the α-β transition at 4.2 K and 0.35 GPa by Thiery *et al.* (26), Raman spectroscopy on polycrystalline α-N_2 at 18 K by Anderson *et al.* (27), theoretical calculation of the pressure dependence of shifts and splittings of Raman active vibrational modes in the α and γ phases by Thiery *et al.* (28) and determination of dynamic structure factor $S(Q,\omega)$ of α nitrogen by Weiss *et al.* (29). Elastic constants of a single crystal of α nitrogen at 15 K have been determined by Kjems and Dolling (24) using phonon dispersion curves obtained from neutron scattering measurements.

The phase diagrams of α and β nitrogen were studied by Swenson (30) using P-V isotherm measurements. Mills *et al.* (31) used P-V-T properties of solid and fluid N_2 up to 2 GPa to measure the sound velocity. Raman spectra from 15 to 30 K at 52 GPa were done by Buchsbaum *et al.*(32). Theoretical calculation of structure and dissociation energy by LeSar *et al.* (33) agrees with experimental lattice constants and energy. On approaching the transition by warming along P=0 isobar, significant mode softening appears above 30 K with an increase in linewidth. Giauque and Clayton (16) showed that the α-β transition is preceded by an anomaly in the specific heat curve indicating the onset of restricted rotation. Kjems and Dolling (24) managed to obtain one single crystal of α phase of 1.5 cm^3 volume and approximately correlated the orientations of α and β phases of nitrogen.

b)CO

Solid CO exists in at least four phases. Ordered primitive cubic

α-CO (space group $P2_13$), disordered hexagonal β-CO (space group $P6_3/mmc$), δ-CO probably disordered cubic (space group Pm3n) and ε-CO possibly rhombohedral (space group R3c). Fig.1.2 shows the phase diagram of CO (13).

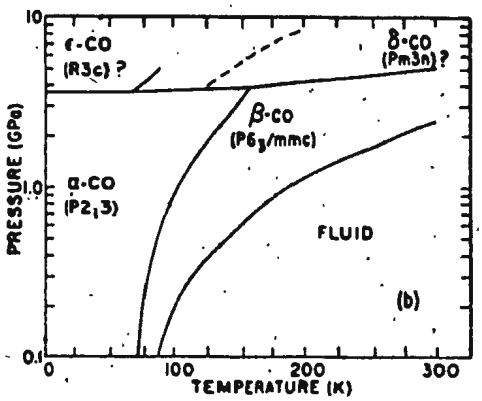

Fig.1.2 Phase diagram of CO.

Single crystals of β-CO grown at room temperature at 2.7 to 3.6 GPa by Cromer *et al.* (34) were examined using x-rays and found to be hexagonal belonging to $P6_3/mmc$ space group. Fukushima, Gibson and Scott (11) determined the α-β transition temperature of CO. They measured the temperature variation of the molar volume in CO which can be used to determine the density at different temperatures. The elastic constants of β-CO at 68 K were determined and compared to β-N_2 by Gammon *et al.* (35) using Brillouin spectroscopy.

Stevenson (36) determined the phase diagram of CO with only two phases using P-V isotherm measurements. Raman scattering on CO from 15 to 297 K and 1 to 5.8 GPa by Katz *et al.* (37) revealed an $\alpha \rightarrow \varepsilon$ transition at 3.4 GPa and $\beta \rightarrow \delta$ at 5.2 GPa at room temperature. Raman spectra of polycrystalline α-CO at 18 K were collected by Anderson *et*

al. (27). Thermodynamic properties of CO having 2.6% N_2 including heat capacity, vapor pressure and heat of transition were determined by Gill and Morrison (38) from 2.5 to 78 K. NMR experiments were also done on β-CO by Fukushima, Gibson and Scott (39). The quadrupole moment of CO being stronger than N_2 is probably the cause for absence of an $\alpha \rightarrow \gamma$ transition in CO (see Raich and Mills (8)).

1-2 Brillouin Scattering

Classically (40) (see also (41)), the thermal motion of molecules create regions of compression and rarefaction which travel in the medium as acoustic waves. This results in propagating fluctuations of the refractive index of the medium. One can think of these fluctuations as plane surfaces which give rise to reflection of incident light. Brillouin scattering is the inelastic scattering of light by the thermally generated density fluctuations in a medium. The frequency spectrum of the scattered light consists of a set of doublets symmetrically situated about the incident light frequency (in liquids, there is one doublet and in single crystals, three doublets). If V is the velocity of sound waves in the medium, the amount of Doppler shift induced in the frequency of incident light due to the movement of plane surfaces is

$$\nu = \frac{2nV}{\lambda} \sin \frac{\alpha}{2} \qquad (1.1)$$

where n is the mean refractive index of the medium, λ is the wavelength of the incident light and α is the scattering angle. The sign of ν depends on the direction of motion of planes relative to the

observer. Equation (1.1) is the famous Brillouin equation.

Quantum mechanically (42) however, the event is considered to be a scattering process of photons by phonons (as noted above). The incident radiation of frequency ω_o and wavevector k_o is scattered by phonons of frequency ω_μ and wavevector k_μ where μ refers to various possible phonon modes as discussed in section 1-4. The incident photon either creates or annihilates a phonon at the scattering site as shown in Fig.1.3.

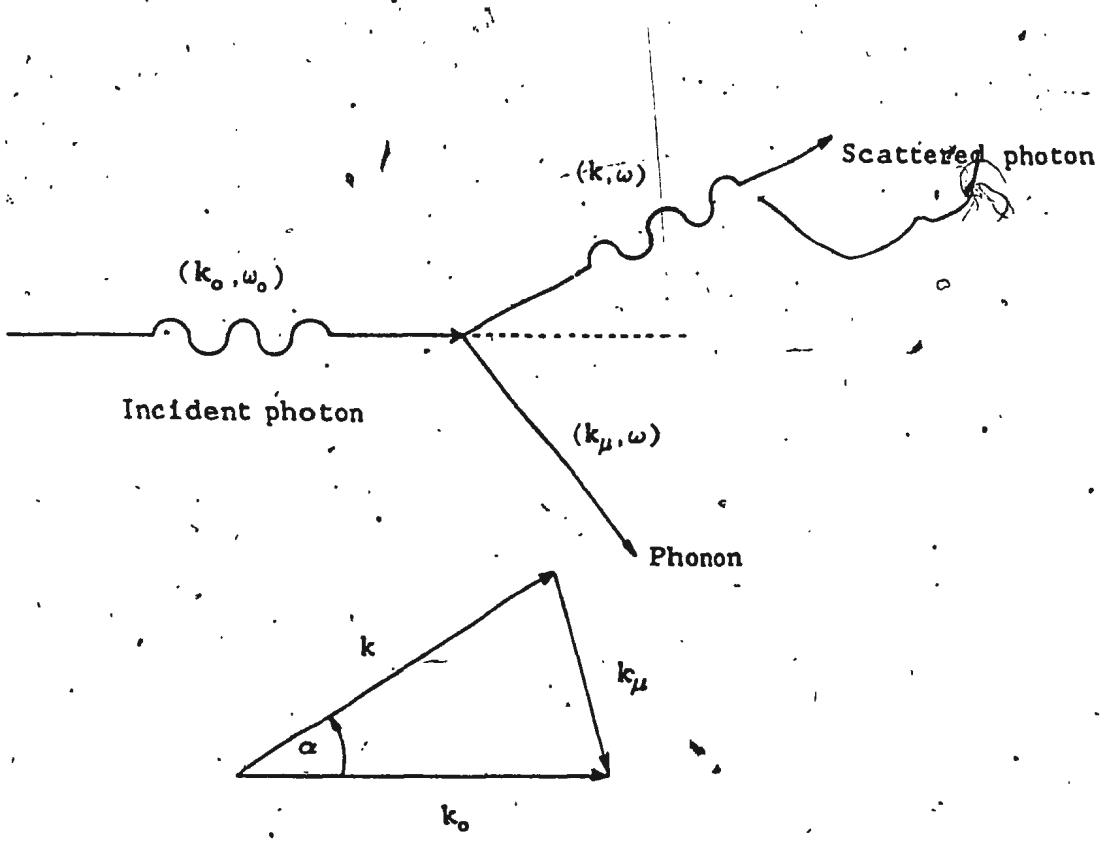

Fig. 1.3 The scattering process of a photon by a phonon.

The following conservation laws hold;

$$\hbar k_o = \hbar k \pm \hbar k_\mu \qquad (1.2)$$

$$\hbar\omega_o = \hbar\omega \pm \hbar\omega_\mu \qquad (1.3)$$

where k and ω are the wavevector and frequency of scattered light. Since $V \ll c$ then $k \approx k_o$ and using Fig.1.3 we can write:

$$k_\mu \approx 2k \sin\frac{\alpha}{2} \qquad (1.4)$$

but $k_\mu = \frac{\omega_\mu}{\nu_\mu}$ and $k = \frac{n\omega}{c}$ for $1/k \gg a$ where a is the interatomic spacing. Therefore eq.(1.4) becomes:

$$\nu_\mu = \frac{2nV}{\lambda} \sin\frac{\alpha}{2}$$

1-3 Stress, Strain And Elastic Constants

The theory of elasticity treats a solid body as a continuum. The relation between internal stresses trying to bring the body back to equilibrium and the amount of deformation is governed by Hooke's law (43).

If under stress, a lattice point at r is displaced to a new position r', the displacement vector is $u = r' - r$; if dl and dl' represent the distances between two points before and after deformation then it is straight forward to show that

$dl'^2 = dl^2 + 2e_{kl}\,dr_k\,dr_l$, where for small deformations e_{kl} becomes:

$$e_{kl} = \frac{1}{2}\left(\frac{\partial u_k}{\partial r_l} + \frac{\partial u_l}{\partial r_k}\right) \qquad (1.5)$$

and is called the strain tensor. We note that $e_{kl} = e_{lk}$. The component of the force acting on one part of body by the rest of it can be written as $F_i = \int_v f_i(r) d^3r$, where f(r) is force per unit volume. These forces are only exerted on the surface enclosing volume V and can be expressed as a surface integral $F_i = \int_A \sigma_{ij} da_j$, where

$f_i(r) = \frac{\partial \sigma_{ij}}{\partial r_j}$. The quantity σ_{ij} is the ith component of the force on a unit area perpendicular to r_j axis and is called the stress tensor.

The relationship between the stress and strain tensor is defined by Hooke's law through a 4th rank elastic constants tensor c_{ijkl} as:

$$\sigma_{ij} = c_{ijkl} e_{kl} \tag{1.6}$$

The strain energy density of a deformed crystal is given by:

$$E = \frac{1}{2} c_{ijkl} e_{ij} e_{kl} \tag{1.7}$$

By introducing a simpler notation whereby pairs of indices are assigned a single label as follows:

Tensor indices	11	22	33	23	31	12
Matrix indices	1	2	3	4	5	6

There are 81 elastic constants in eq.(1.6). Using symmetry relations for σ_{ij} and e_{kl}, the number of independent elastic constants become 36 and using eq.(1.7), they are further reduced to 21. For the hexagonal

close-packed structure, there is a six-fold symmetry about z axis which reduces the elastic constants further to five i.e. c_{11}, c_{12}, c_{13}, c_{33} and c_{44}. The elastic constant matrix becomes:

$$|c_{ij}| = \begin{bmatrix} c_{11} & c_{12} & c_{13} & 0 & 0 & 0 \\ c_{12} & c_{11} & c_{13} & 0 & 0 & 0 \\ c_{13} & c_{13} & c_{33} & 0 & 0 & 0 \\ 0 & 0 & 0 & c_{44} & 0 & 0 \\ 0 & 0 & 0 & 0 & c_{44} & 0 \\ 0 & 0 & 0 & 0 & 0 & \frac{(c_{11}-c_{12})}{2} \end{bmatrix}$$

For cubic crystals, the cubic symmetry reduces the number of elastic constants from 21 to three i.e. c_{11}, c_{12} and c_{44}. The elastic constant matrix becomes (44):

$$|c_{ij}| = \begin{bmatrix} c_{11} & c_{12} & c_{12} & 0 & 0 & 0 \\ c_{12} & c_{11} & c_{12} & 0 & 0 & 0 \\ c_{12} & c_{12} & c_{11} & 0 & 0 & 0 \\ 0 & 0 & 0 & c_{44} & 0 & 0 \\ 0 & 0 & 0 & 0 & c_{44} & 0 \\ 0 & 0 & 0 & 0 & 0 & c_{44} \end{bmatrix}$$

1-4 Propagation Of Waves In Hexagonal Crystals

The force per unit volume $f(r)$ and the displacement vector u are related by Newton's second law of motion: $f = \rho \frac{d^2 u}{dt^2}$, where ρ is the crystal density. The ith component of this equation is :

$$\sum_j \frac{\partial \sigma_{ij}}{\partial x_j} = \rho \frac{d^2 u_i}{dt^2} \qquad (1.8)$$

Using Hooke's law and eq. (1.5) we can write:

$$\sum_{ijk} c_{ijkl} \frac{\partial^2 u_l}{\partial x_j \partial x_k} = \rho \frac{d^2 u_i}{dt^2} \qquad (1.9)$$

which is the differential equation for wave propagation and has a solution of the form : $u_i(r,t) = u_{io} e^{i(k.r-\omega t)}$ (I.10)

where u_{io} is the amplitude of propagation. Substituting eq.10 in eq.9 and rearranging we obtain:

$$\sum_i (\sum_{jk} c_{ijkl} k_j k_k - \rho\omega^2 \delta_{il}) u_{io} = 0 \qquad (1.11)$$

The determinant of the matrix $\sum_{jk} c_{ijkl} k_j k_k - \rho\omega^2 \delta_{il}$ must vanish for non-trivial solutions. The solution of this secular equation yields expressions for ω^2. For hexagonal crystals the final solutions for propagating velocities are:

$$\rho v^2(L) = \frac{1}{2}\left[(c_{11}+c_{44})\sin^2\gamma + (c_{33}+c_{44})\cos^2\gamma + \Phi\right]$$

$$\rho v^2(T_1) = \frac{1}{2}(c_{11}-c_{12})\sin^2\gamma + c_{44}\cos^2\gamma \qquad (1.12)$$

$$\rho v^2(T_2) = \frac{1}{2}\left[(c_{11}+c_{44})\sin^2\gamma + (c_{33}+c_{44})\cos^2\gamma - \Phi\right]$$

where $\Phi^2 = [(c_{11}-c_{44})\sin^2\gamma + (c_{44}-c_{33})\cos^2\gamma]^2 + 4\sin^2\gamma\cos^2\gamma(c_{13}+c_{44})^2$

and γ is the angle between k and the c axis.

Thus there are three types of waves propagating , a pure transverse T_1, a quasi-transverse T_2 and a quasi-longitudinal L which are distinct in single crystals.

1-5 Euler Angles

The three Euler angles are defined in the standard way, per Goldstein (45), as ϕ about the body z axis, θ about the line of nodes and χ about the body z axis; all the rotations are counter clockwise. The rotation matrix from the body to the space coordinate system then is given by:

$$A = \begin{bmatrix} \cos\chi\cos\phi-\cos\theta\sin\phi\sin\chi & -\sin\chi\cos\phi-\cos\theta\sin\phi\sin\chi & \sin\theta\sin\phi \\ \cos\chi\sin\phi+\cos\theta\cos\phi\sin\chi & -\sin\chi\sin\phi+\cos\theta\cos\phi\cos\chi & -\sin\theta\cos\phi \\ \sin\chi\sin\theta & \cos\chi\sin\theta & \cos\theta \end{bmatrix} \quad (1.13)$$

Any vector X in the body frame of reference can be transformed to the space frame of reference X' by: $X' = AX$, where X and X' can be expressed as column matrices of the form $\begin{bmatrix} a \\ b \\ c \end{bmatrix}$ where a, b and c are constants.

1-6 Phase Transformations

Any phase transformation requires a change in the arrangement of the atomic structure of the material (46). These changes are made by driving forces; the atoms assume new positions under the influence of strain energy, surface energy or external stress even though the free energy of one structure is lower than that of the other.

The transformations can be divided into homogeneous and heterogeneous. The homogeneous transformation takes place in all parts

of the assembly at the same time, whereas, in the heterogeneous transformation one can distinguish microscopically distinct transformed and untransformed regions. The heterogeneous transformation is divided into two groups depending on the reaction velocity and amount of transformation with temperature and time. The experimental classification corresponds to an actual difference in the mechanism of the transformation. The two groups are known as "nucleation and growth" reactions and "martensitic" reactions. In the first group, the new phase grows out of parent phase by slow migration of the interface boundary. The growth then results from independent atom-by-atom transfer across the boundary. The reaction continues isothermally at a given temperature and the amount of new phase increases with time. The second kind of heterogeneous transformation occurs only in solids and proceeds by the cooperative movement of many atoms. Most atoms have the same nearest neighbors in both phases. Discrete regions of solid transform with very high velocity which is independent of temperature. In most cases, the amount of transformation is characteristic of temperature and does not increase with time. Reactions of this kind are called "shear" or "diffusionless" transformations but they are also referred to as "martensitic" transformations. The alternate division is based on the analogy between the different mechanisms of transformation and the way in which soldiers and civilians respectively carry out certain tasks like getting into a train. Thus the main categories of the heterogeneous transformations are called "military" (i.e. martensitic) and "civilian" (i.e. nucleation and growth).

The main characteristics of martensitic reactions are (see also (47)):

a) The amount of transformation is independent of time. A fraction of the parent phase transforms very rapidly and at a certain temperature there is usually no further transformation. This is a primary characteristics of the martensitic transformation.

b) The amount of transformation varies with temperature if other variables such as grain size are maintained constant. The velocity of transformation is probably independent of temperature and is very rapid. Transformation begins suddenly at a fixed temperature T_1 and as the temperature is varied, more of crystal transforms until the temperature T_2 is reached at which the transformation is complete.

c) Martensitic reactions are reversible. By heating and cooling the crystal successively, initial atomic configuration can be repeatedly obtained. A single crystal of the original phase can transform to a single crystal of the daughter phase. Reversing the process results in a single crystal of the original phase having same orientations.

d) The amount of transformation can increase if plastic stresses are applied between T_1 and T_2 and can even be brought to completion. The direction of the applied stress is important for single crystals and some reactions may be retarded or accelerated by a stress in a suitable direction.

e) The transformed crystal has the same chemical composition as the parent phase. Little or no volume changes are involved (0.3% in Co).

f) There exists a definite relation between the orientations of the parent structure and that of the daughter phase.

g) It is believed that α-β transitions in N_2 and CO are of the martensitic type.

CHAPTER 2

EXPERIMENTAL SETUP AND PROCEDURE

The experimental setup for Brillouin spectroscopy studies of single crystals is shown in Fig.2.1. A single-mode argon laser beam was incident on the cell inside a specially designed cryostat. The scattered beam was analyzed at 90° by a piezoelectrically scanned Fabry-Perot interferometer. The light was collected by a photomultiplier tube and stored in a data acquisition and stabilization system. X-rays are used to obtain Laue diffraction patterns of the crystals. A He-Ne beam defined the scattering axis.

2-1 Laser Source

Highly monochromatic laser radiation is necessary in the technique of high resolution Brillouin spectroscopy. A 4 W single mode argon ion laser (Spectra Physics 165) was used. With an intracavity prism, the action of the laser is tuned to the 514.5 nm line. The line has a Doppler broadened width of about 5 GHz within which several axial modes oscillate with a separation of 115 MHz. An intracavity Fabry-Perot etalon is used to select a single axial mode. Because of "jitter" due to microphonics, the effective linewidth is about 15 MHz and ultimately is the limiting factor in the experimental resolution. To further mechanically stabilize the laser, it was mounted on a steel table bearing a large granite block which was separated from the floor by rubber mountings. For the present experiment, a power of 20 mW was used in order to prevent the crystal from being destroyed by heating

effects.

2-2 The Optical System And Alignment

The arrangement of the optical system is shown in Fig.2.1. The incident beam passes through pinhole P_1 and a high quality quartz lens L_1 of focal length 35 cm. A front surface mirror deflects the beam vertically through the centre of the cell through aperture P_2. The scattered beam, having its solid angle ($\sim 5 \times 10^{-6}$ steradians) defined by pinhole P_3 is rendered parallel by a high quality antireflection coated lens L_2 of focal length 40 cm and is incident on the front plate of the Fabry-Perot (Burleigh RC 110). The transmitted light from the Fabry- Perot is focused by quartz lens L_3 of focal length 80 cm onto pinhole P_4 (of diameter 400 μ) and finally to the photocathode of a photomultiplier tube (ITT FW 130) which is thermoelectrically cooled and has a dark count of less than 1 per second. The electrical output is fed through an Amplifier/Discriminator into the Data Acquisition and Stabilization system (Burleigh, DAS-1) which will be discussed later.

The triple pass Fabry-Perot interferometer consists of two optically flat parallel plates separated by a certain distance d. The opposing faces are coated with partially reflecting films (93% reflectivity in this experiment). The distance d determines the wavelength transmitted by the Fabry-Perot. A ramp voltage across the three piezoelectric transducers on one of the plates scans the frequency. The free spectral range F.S.R. (11.617 GHz in this experiment) is the frequency difference between two successive orders of the Fabry-Perot transmission and is given by FSR = $\frac{c}{2nd}$ where c is the velocity of light and n is the refractive index. The finesse F is

Fig. 2.1 The optical arrangement for the Brillouin scattering and x-ray diffraction analysis of N_2 and CO.

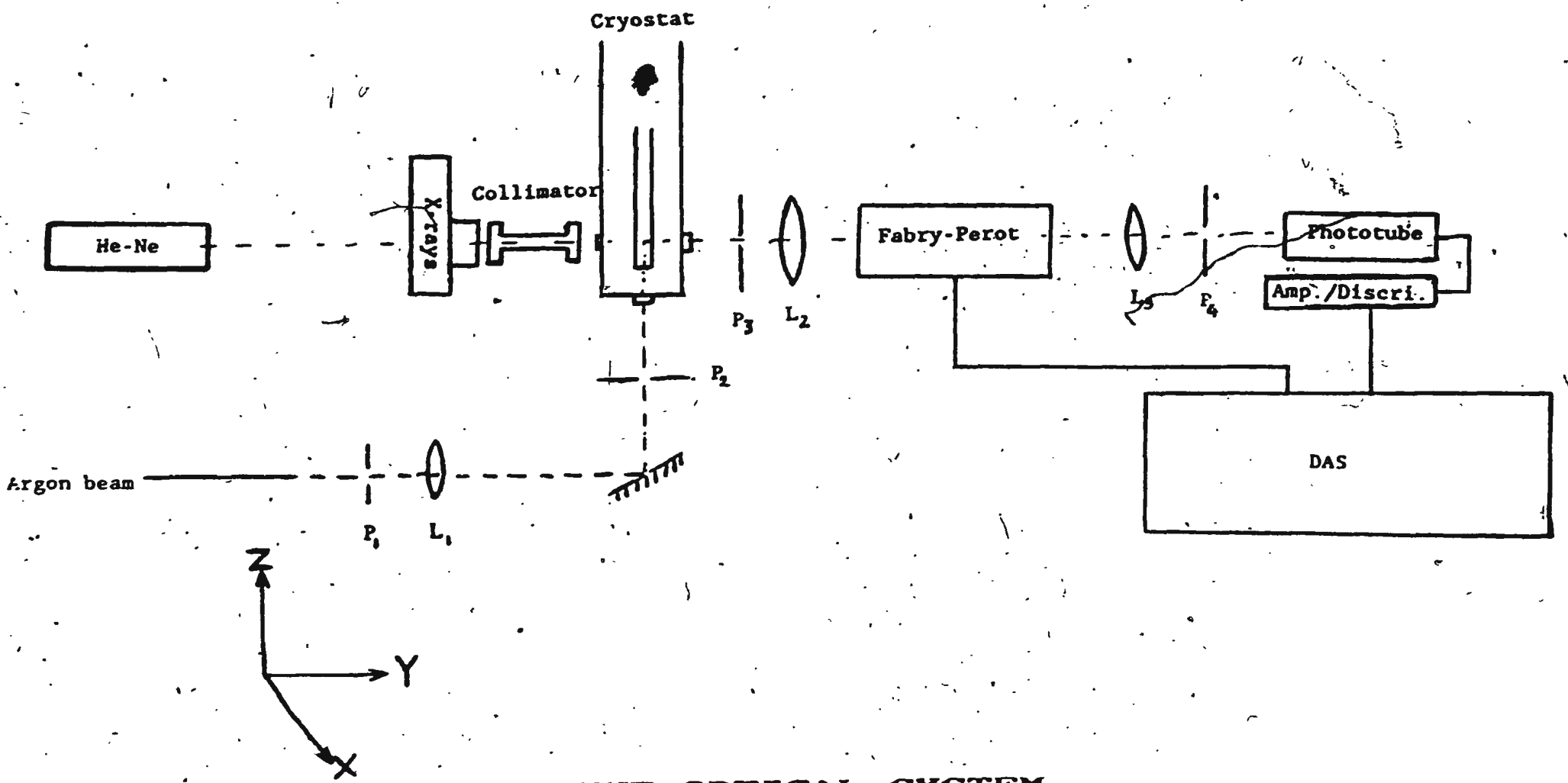

THE OPTICAL SYSTEM

Fig. 2.1

defined as the ratio of F.S.R. to the minimum resolvable linewidth (i.e. Fabry-Perot instrumental width). A higher finesse therefore indicates a better resolution of closely spaced lines for a given F.S.R. The finesse is determined by plate flatness and reflectivity and is about 60 in this experiment.

A He-Ne beam is first aligned into the phototube to define the optical axis of the system with no other optical element present. Then the lenses, Fabry-Perot and pinholes are added in sequence so as not to deviate the beam. The Fabry-Perot is set on single pass and by observing the "sharpness" of its transmission is adjusted manually, first on the He-Ne beam and then on the argon beam scattered from a piece of card. The Fabry-Perot is aligned more accurately on single pass by using the piezoelectric bias on the DAS-1 and by maximizing the DAS-1 signal. Then retroreflector is rotated into the 3 pass mode and the Fabry-Perot is finely tuned again by maximizing the signal on the DAS-1. A pentaprism is used to ensure that the incident argon beam is exactly at 90° to the He-Ne defined scattered direction.

2-3 DAS SYSTEM

The Data Acquisition and Stabilization system serves several functions. It provides a bias signal to the piezoelectric transducers of the Fabry-Perot interferometer for parallel adjustment of the mirrors and the appropriate scanning voltage from .01 to 99.99 ms per channel using a digital high voltage sweep. It accumulates in memory via a 1024 channel multichannel analyzer, the 1 volt pulses put out by the Amplifier/Discriminator corresponding to each detected photon. It further corrects automatically for the frequency drift of the laser or

any other frequency drifts by locking a particular spectral feature (such as the Rayleigh line) to a preselected channel number and keeps it centered there. It can also be programmed to keep the Fabry-Perot plates parallel and continuously maximize the finesse. Another feature of the DAS is the segmented option which allows for amplification (up to 100 times) of any part of the spectra by spending more time per channel in preselected sections of the ramp. This is important when searching for very weak spectral features. A spectrum of intensity versus frequency is continuously displayed on the multichannel analyzer CRT and an adjustable "cursor" provides for alphanumeric readout of photon counts and channel number.

2-4 Cryostat

The cryostat (Fig.2.2) is the one that was used by S.F.Ahmad (48) (see also (49)). The outer body of the cryostat (26) was made of thin stainless steel. It contains two reservoirs: one for liquid nitrogen (8) which was automatically refilled every 6 hours and one for liquid helium (9) filled every two days. The cell, soldered to a long stainless steel tube, was suspended in the central bore of the cryostat and centered vertically by a teflon spacer (21). The top part of it was connected to a brass tube (1) through which the sample comes to the cell. The rotation of the cell is carried through rotary seals (29), (31) with a scale to read the degree of rotation. The liquid helium from the reservoir (9), after passing through the capillary tube (22) reaches to the heat exchanger can (20). A needle valve having a control knob at the top (28) regulates the flow of the helium. Liquid helium after falling to the bottom of the heat exchanger, is vaporized

Fig.2.2. Diagram showing the top and the tail section of the cryostat

1 -Brass inlet tube

2 -Stainless steel tube

3 -Rubber O-rings

4,5 -Port for He recovery from the heat exchanger and He reservoir

6,27 -Liquid He and nitrogen fill

7 -Space under vacuum

8,9 -Liquid nitrogen and helium reservoirs

10,13 -Radiation shields

11 -Dust collector assembly

12 -Heater wires

14 -Aluminum foil

15 -Plexiglass large window

16 -Quartz sample cell

17 -Polished quartz window

18 -Plexiglass small window

19 -Copper braids

20 -Heat exchanger can

21 -Teflon spacer

22 -Liquid helium capillary tube

23,28 -Needle valve and its control knob

24 -Cryostat pumping port and electrical feedthrough

25 -Thermal anchor

26 -Polished stainless steel outer wall of the cryostat

29 -Rotary seal for rotating the sample cell

30 -Electrical feedthrough for temperature and gradient measurment

31 -Assembly for raising or lowering the cell

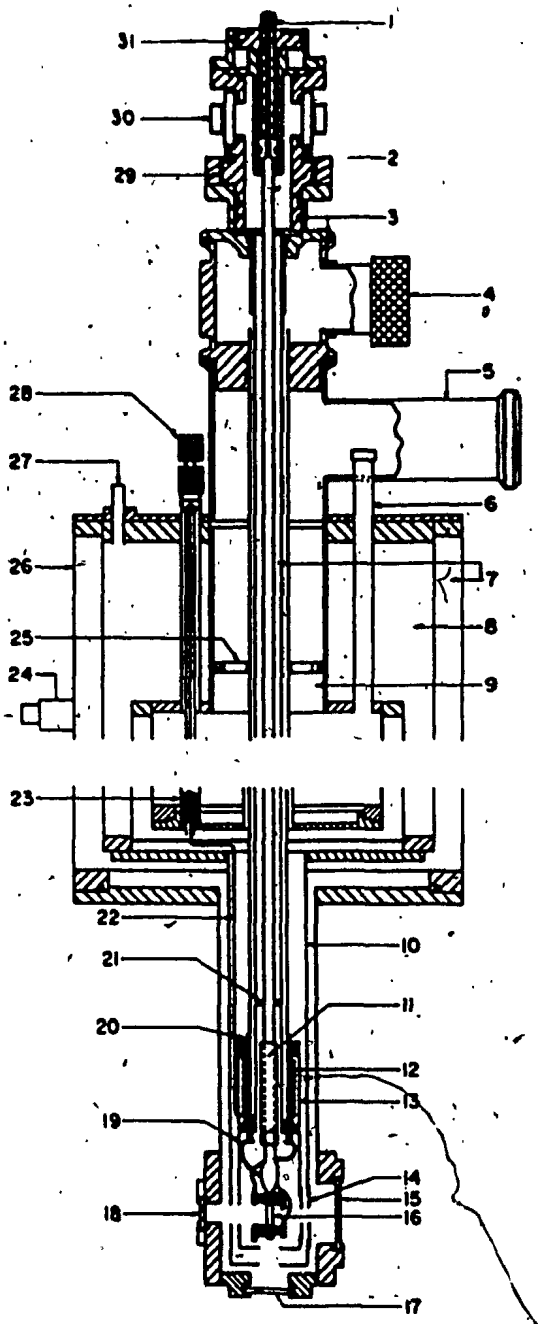
1
31
30
29
2
3
4
5
28
27
6
26
7
8
25
24
9
23
22
10
21
11
20
12
13
19
14
15
18
16
17

Fig. 2.2

and the cool vapor circulates upward to escape through the outlet (4) into the helium return system. Two brass rods are projected downwards from the bottom sides of the heat exchanger and serve as the cold finger. These are connected to the copper braids from the cell (19). A heater (12) is used to control the temperature of the cold finger in conjunction with a GaAs temperature sensor and proportional control circuit. There are two aluminum shields surrounding the cell. The inner shield (13) was maintained at the same temperature as the heat exchanger and the outer shield (10) at liquid nitrogen temperature. There are windows around the cell, one made of quartz (17) through which beam enters. The window (15) through which the scattered light passes and the window (18) where made of plexiglass to allow x-ray transmission. The cryostat rested on an aluminum plate which could be adjusted by means of three leveling screws. The plate was finely adjustable allowing for the cryostat to be moved across the beam passing through the cell. This was added since Ahmad's work.

2-5 Cell

The cell (Fig.2.3) is a quartz tube of inner diameter 3 mm and outer diameter 5 mm and length of about 2 cm and was fitted with a quartz to Kovar graded seal at the top. A dust trap between the cell and the inlet tube prevents dust particles settling at the bottom of the cell. The bottom of the cell was closed by a polished fused quartz plug glued to the cell by epoxy resin. A phosphor bronze clip was clamped to the lowest part of the cell. This clamp had a miniature GaAs diode mounted on it. One side of the clamp was folded to provide housing for a differential thermocouple. Another clamp was fastened to

Fig. 2.3 Detailed diagram of the sample cell where crystal growth and cooling was carried out.

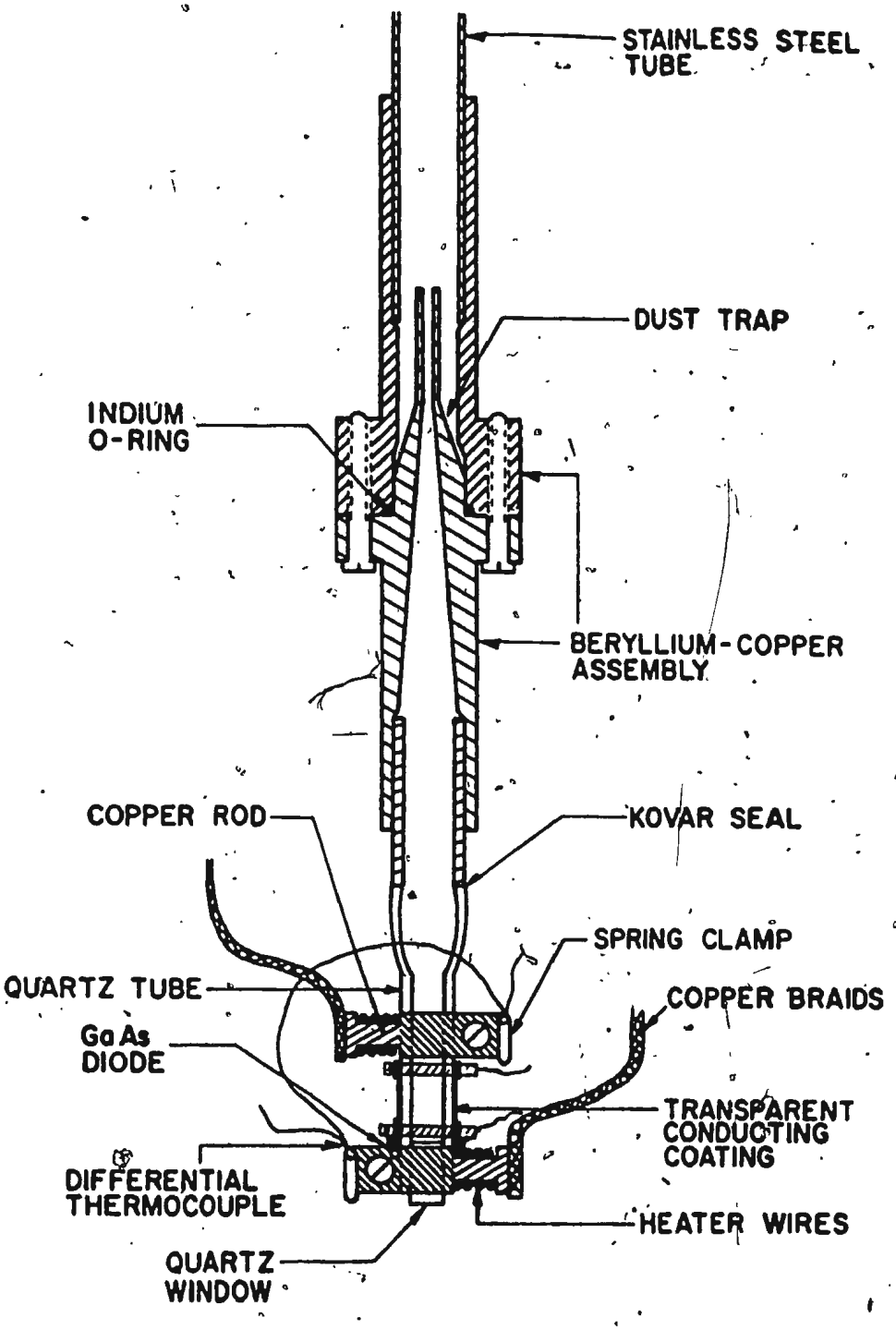

SAMPLE CELL

Fig. 2.3

the cell above the first and provides for the second junction of the thermocouple. To each clamp, two copper rods were soldered and joined to one end of a copper braid. The other end of the copper braid was connected to the cold finger of the heat exchanger. Wires wound on each rod provide for the control of the cell temperature.

A major modification made to this system since Ahmad's Ph.D. work (48) involved the deposition of a thin, optically transparent, electrically conducting coating on the cell body between the clamps. The film has a 70% transmission coefficient and 10 ohms electrical resistance and is about 1 cm high. Two thin brass clamps, lined inside with indium, were used for electrical contact to the film. Teflon rings were used to isolate these clamps from the rest of the system (i.e. above mentioned phosphor bronze cooling clamps). This film is used when the crystals are being cooled i.e. electrical current is passed through the film to release the crystals from the walls of the cell.

2-6 Temperature Control

The cell temperature is affected in four ways:

i) an externally controlled needle valve regulates the rate of flow of liquid helium in the heat exchanger can,

ii) temperature at the bottom of the can is finely controlled to about 4 K below cell temperature by proportional electronic control using the GaAs diode and heater system,

iii) temperature at the bottom of the cell is controlled using a similar proportional electronic control assembly,

iv) temperature at the top of the cell and hence temperature gradient in cell is controlled via differential thermocouple and heater

proportional control system.

2-7 Crystal Growth And Cooling Procedure

The nitrogen or carbon monoxide gas inside the cell was cooled until the liquid state was obtained. The liquid was then cooled manually to about a degree above the triple point temperature. The crystals were grown by maintaining a gradient of about 2.5 K between the top and the bottom clamps (with the top being warmer) and lowering the temperature automatically by about 0.05-0.1 K per hour until a small (0.05 mm) seed was formed at the bottom of the cell. The seed was then grown slowly for a about day until a large single crystal was obtained. Many crystals were melted at this point mainly because of their short range of angle γ. A large γ range is necessary to meaningfully determine all five elastic constants.

Appropriate crystals of good quality were further cooled automatically for another day to ensure that the they would not melt during cooling process. This process is a combination of heating the walls of the cell and simultaneous pumping on the crystal. The liquid on the top of crystal was removed completely and the remaining crystal was reduced in size by pumping very slowly on the cell. The film voltage was raised to 1.6 volts in steps of 0.2 each hour. Sudden increase in film temperature would melt the crystal and enough time had to be given for the equilibrium state to be established. Controlled excess energy in the film melted the crystal at the boundary with the walls of cell and the liquid formed was removed by pumping. Eventually when the crystal was released from the walls, having a dome-shape appearance, it was cooled quickly (at about 8 K an hour) to the desired

temperature. For nitrogen (because of the larger temperature range), the above mentioned process was carried out three times whereas for CO, once was sufficient to cool it to the appropriate temperature just above the triple points. When the cooling was over, the pump was removed and the gap between the crystal and the walls of the cell began filling with solid, and the crystal would grow slightly. The film temperature was then lowered by reducing the heater voltage to 1.2 volts in steps of 0.1. Keeping the film temperature fairly high allowed for a better (more strain free) phase transition involving volume expansion. The key factor in the success of this operation was to find a proper ratio between the rate of pumping and the rate of increasing the film voltage.

Further cooling through the phase transition was carried out extremely slowly (about 0.05 K per hour). The cooling was stopped periodically for several hours to check the crystal and allow it to come to equilibrium.

2-8 Crystal Orientation Procedure

Laue x-ray transmission diffraction is used to determine whether a crystal is single and to determine its orientations relative to the laboratory frame of reference. The pattern typically consists of several well defined spots surrounding a central spot due to the undiffracted beam. By observing the pattern and shape of spots, it is possible to estimate the quality (degree of strain and polycrystalline nature) of the crystals. This procedure has been completely computerized in this laboratory (initially by Gammon (10)) and is based on stereographic projection techniques (50). An accurate measurement of

the coordinates of the Laue spots is necessary and fed into the computer which determines the Euler angles and Miller indices. Each spot is always accounted for. It is important that consistent orientations are obtained as crystal is rotated i.e. only the ϕ angle is changed. The orientation of each crystal with respect to the laboratory frame of reference in Euler angle notation (θ, ϕ, χ) was determined using this technique.

The x-ray equipment used was a Philips MO 100/Be 100 Kv beryllium window tube. The beam was passed through a lead collimator and then through the crystal. The diffraction pattern was recorded on Polaroid 57 film in an XR-7 Land camera, perpendicular to the direction of the incident x-rays and at a distance of 8.4 cm from it.

2-9 Measurement Of Spectra

The Brillouin spectra of different crystals were recorded on the DAS CRT screen and a sample spectrum is shown in Fig.3.1. in chapter 3. The "cursor" was used which when addressed to a specific channel on the CRT screen, could measure the number of counts and channel number at the various peaks. Three Rayleigh peaks were usually recorded. Referring to Fig.2.4, the spectral free range Δ, was the mean of Δ_1 and Δ_2 in channel numbers. This corresponds (in this experiment) to a S.F.R. of 11.716 GHz of the Fabry-Perot (ν=11.617 GHz). The average recorded frequency shifts for the various shifts were obtained over the two spectral orders for a particular spectral component by multiplying their mean shift by ν(S.F.R.)/Δ.

In the case of extremely weak signals (such as some transverse components) a segment extending from a Rayleigh peak to the nearest

Fig. 2.4 Different components of the spectra are shown. The R's are the central components (Rayleigh lines). The L's and T's are the longitudinal and transverse components of the correspondingly dashed R's. Δ' are the shifts of various components in GHz.

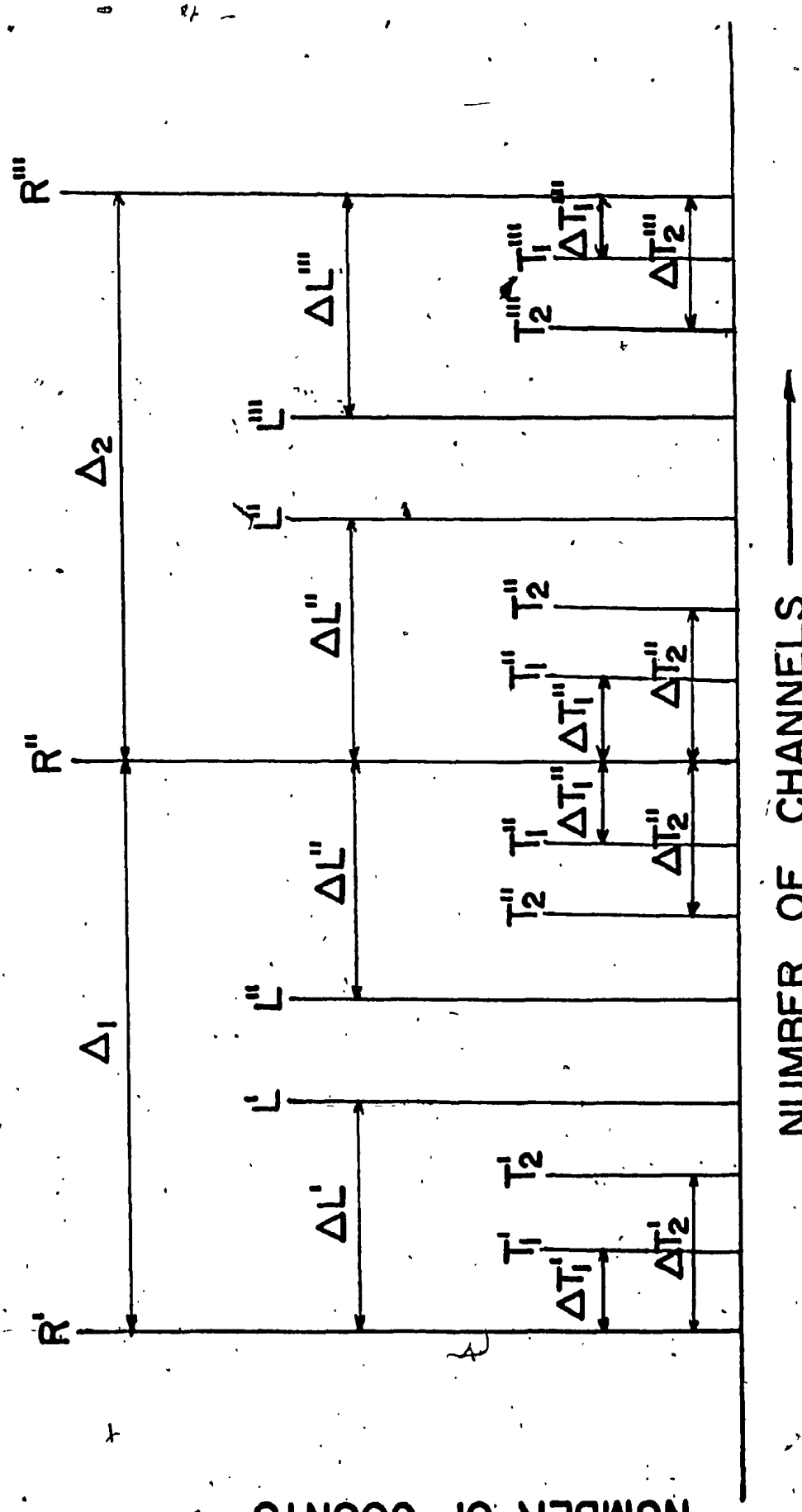
NUMBER OF COUNTS
NUMBER OF CHANNELS
(MAX. = 512)
R'
R''
R'''
L'
L''
L'''
Δ1
Δ2
ΔL'
ΔL''
ΔL'''
T1'
T2'
ΔT1'
ΔT2'
T1''
T2''
ΔT1''
ΔT2''
T1'''
T2'''
ΔT1'''
ΔT2'''

Fig. 2.4

longitudinal peak was placed. The DAS would then spend most of the time passing through the segmented region and record weak signals. The frequency shifts were then obtained by finding the relative shift of transverse component with respect to the longitudinal component. If ΔT^* is the shift of transverse component and ΔL^* the shift of longitudinal component in the segmented region, then the actual transverse shift is $\Delta T = \Delta T^* \frac{\Delta L}{\Delta L^*}$ where ΔL is the mean longitudinal shift outside the segmented region.

CHAPTER 3

EXPERIMENTAL RESULTS AND ANALYSIS

3-1 Brillouin Spectra Of β-CO And β-N_2

a) Spectrum of β-CO

A spectrum of β-CO is shown in Fig. 3.1. There were three Rayleigh lines (R) recorded which were the most intense spectral feature. There were two longitudinal components (L), an upshifted and a downshifted, symmetrically situated about the central Rayleigh peak. One of the transverse components (T_2) could be recognized readily and the other transverse component (T_1) appeared infrequently and weakly on the segmented ramp portion of the scan. The transverse modes were both weak and the amount of shift was small. At low and high γ angles, the transverse modes were closer together and became harder to observe and resolve. No attempt was made to correlate the intensities at the time of collecting the spectra. The longitudinal components were about 150 times weaker than the Rayleigh and about ten times stronger than the transverse. Measurements were also made of the spectra at the triple point which were consistent with Gammon's results (35). Low input laser power was used (10 mW) to avoid melting crystals just above the phase transition

b) Spectrum of β-N_2

The spectrum of β-N_2 was similar to the spectrum of β-CO. However, both transverse components were observed more frequently and the shifts were slightly larger than the shifts in β-CO. Longitudinal components

Fig. 3.1 The spectrum of β-CO at 62 K. The second transverse component was very weak and did not appear at (70.7,354.9,119.3) orientation.

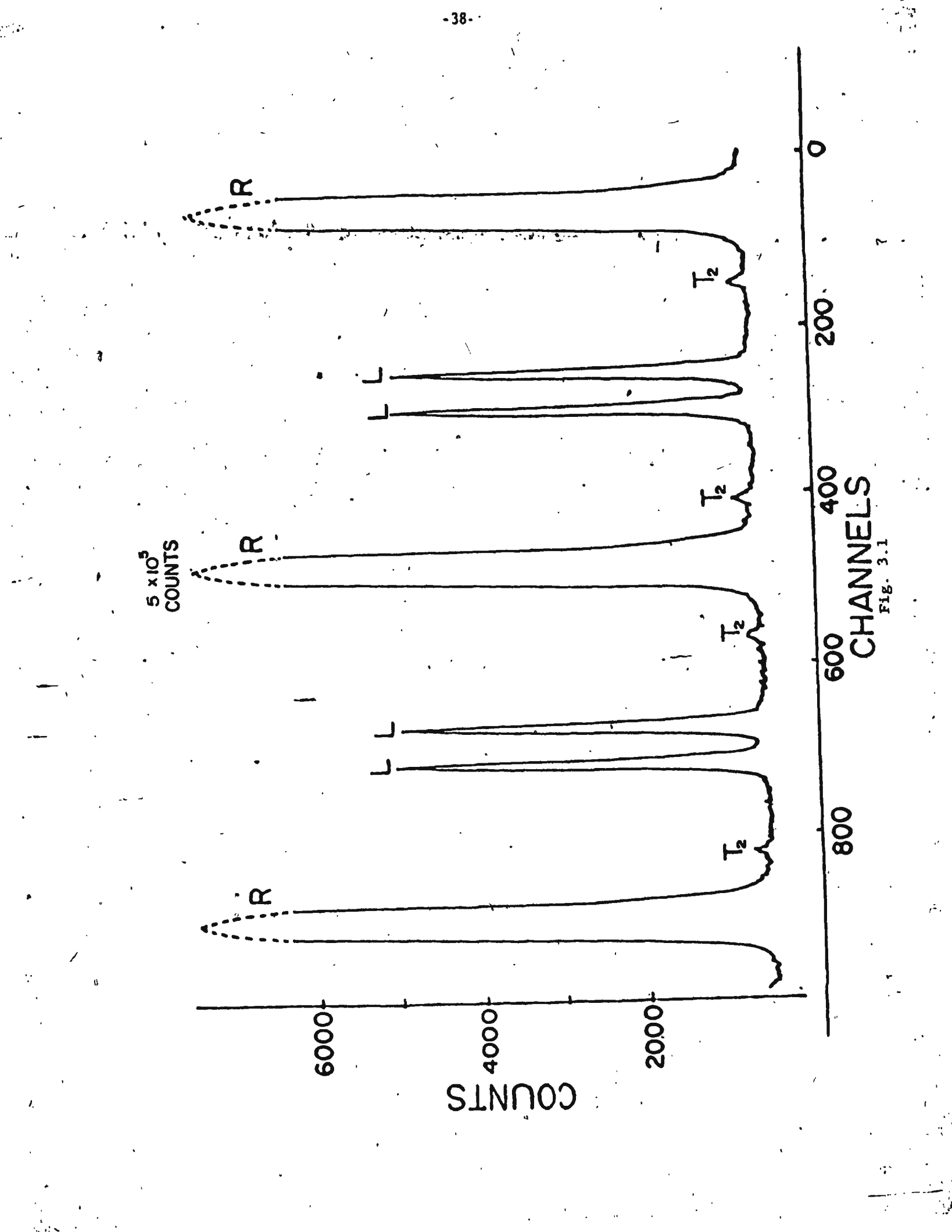
COUNTS
6000
4000
2000
5 x 10³ COUNTS
R
L
L
T₂
T₂
R
L
L
T₂
T₂
R
T₂
0
200
400
600
800
CHANNELS

Fig. 3.1

peaks were about 100 times weaker than the Rayleigh and seven times stronger than the transverse components. The input laser power used was about 20 mW.

In both cases the linewidths were instrumental, that is, determined by the Fabry-Perot finesse such that linewidth $\approx \frac{S.F.R.}{F}$ $\approx$ 200 MHz.

3-2 Elastic Constants

a) β-CO

The elastic constants of β-CO were measured using the expressions for frequency shift (1.1) in terms of sound velocity and sound velocity in terms of elastic constants (1.12). Four single crystals of β-CO were cooled to within a degree above the phase transition. 16 spectra at different orientations were recorded (Table 3.1). Fortunately, the T_1 component was observed several times allowing for the determination of c_{12} (which appears only in the expression of T_1 velocity).

A knowledge of density and refractive index is essential in determining the elastic constants. The density used for CO was obtained from a paper by Gibson and Scott (11) from their molar volume graph. They measured the temperature dependence of molar volume of CO and N_2 from 50 K to 4 K. The density for CO just above the phase transition was 0.921 ± 0.012 gm/cm^3. There was no measured value of the refractive index of solid CO in the literature. However, the refractive index at the triple point has previously been calculated (35) via the Lorentz-Lorenz relation using measured values of liquid refractive index (51) and density (11). Knowing the density of the cooled crystal allows one to calculate the refractive index using the Lorentz-Lorenz

TABLE 3.1

Observed and calculated "best-fit" frequency shifts as a function of orientation for four CO single crystals at 62 K

Crystal	Euler Angles			Observed Frequency Shift in GHz			Calculated Frequency Shift in GHz		
#	θ	ϕ	χ	$\nu(L)$	$\nu(T_2)$	$\nu(T_1)$	$\nu(L)$	$\nu(T_2)$	$\nu(T_1)$
CO1	71.1	219.9	248.0	5.002	2.265	-	5.071	2.278	2.410
	71.1	199.9	247.5	5.024	2.701	2.256	5.044	2.510	2.279
	71.1	249.9	248.9	5.044	-	2.359	5.108	2.283	2.278
	69.8	239.9	248.5	4.980	-	2.321	5.104	2.296	2.278
CO2	115.4	108.4	112.8	5.028	2.620	-	5.024	2.602	2.279
CO3	96.0	118.7	255.5	5.078	-	-	5.041	2.522	2.279
	96.0	138.7	255.9	5.092	-	-	5.019	2.667	2.280
	96.0	138.7	255.9	5.014	-	-	5.019	2.667	2.280
	96.0	148.7	256.3	5.060	-	-	5.033	2.691	2.280
	96.0	158.7	256.4	5.093	-	-	5.055	2.688	2.281
	96.0	158.7	256.4	5.081	-	2.264	5.055	2.688	2.281
CO4	70.7	354.9	119.3	5.244	-	2.237	5.212	2.526	2.282
	70.7	354.9	119.3	5.243	2.589	2.234	5.212	2.526	2.282
	70.7	324.9	123.7	5.135	-	-	5.087	2.666	2.281

TABLE 3.1 continued

Crystal	Euler Angles			Observed Frequency Shift in GHz			Calculated Frequency Shift in GHz		
	θ	ϕ	χ	$\nu(L)$	$\nu(T_2)$	$\nu(T_1)$	$\nu(L)$	$\nu(T_2)$	$\nu(T_1)$
	70.7	324.9	125.1	5.078	2.585	-	5.087	2.666	2.281
	70.7	344.9	120.3	5.161	2.524	-	5.185	2.560	2.282

relation:

$$\frac{n^2-1}{n^2+2} = \rho L$$

where L is the Lorentz function and is assumed to be constant. This gives a value of 1.257±0.023 for the refractive index of CO at 62 K. The elastic constants were calculated from the measured frequency shifts using the following computerized iteration procedure. Initial values of elastic constants were assumed and the frequency of the three modes for all the various crystal orientations were calculated using (1.12). A least-square fitting procedure minimized the difference between the calculated and measured frequency shifts and thus "corrected" the assumed elastic constants. This procedure was repeated and iterated until a value of $\chi^2 = 1.00$ was obtained. The final elastic constants are therefore the ones that best-fit the calculated shifts to the observed shifts.

The best-fit adiabatic elastic constants for CO at 62 K in units of 10^9 N/m^2 are:

$c_{11} = 2.013 \pm 0.020$ $\quad c_{12} = 1.212 \pm 0.025$ $\quad c_{13} = 0.998 \pm 0.026$

$c_{44} = 0.402 \pm 0.016$ $\quad c_{33} = 2.227 \pm 0.034$

The bulk modulus is given by the following expression:

$$B = \frac{(c_{11}+c_{12})c_{33}-2c_{13}^2}{c_{11}+c_{12}-4c_{13}+2c_{33}}$$

and was calculated to be 1.407 in the same units.

The above errors were determined by the quality of the fit and express the experimental self consistency corresponding to a single

Fig. 3.2 The change in frequency shift with angle γ. The solid curve is a fit to the elastic constants of β-CO at 62 K. The dotted curve is a fit to the elastic constants at 68 K obtained by Gammon (35).

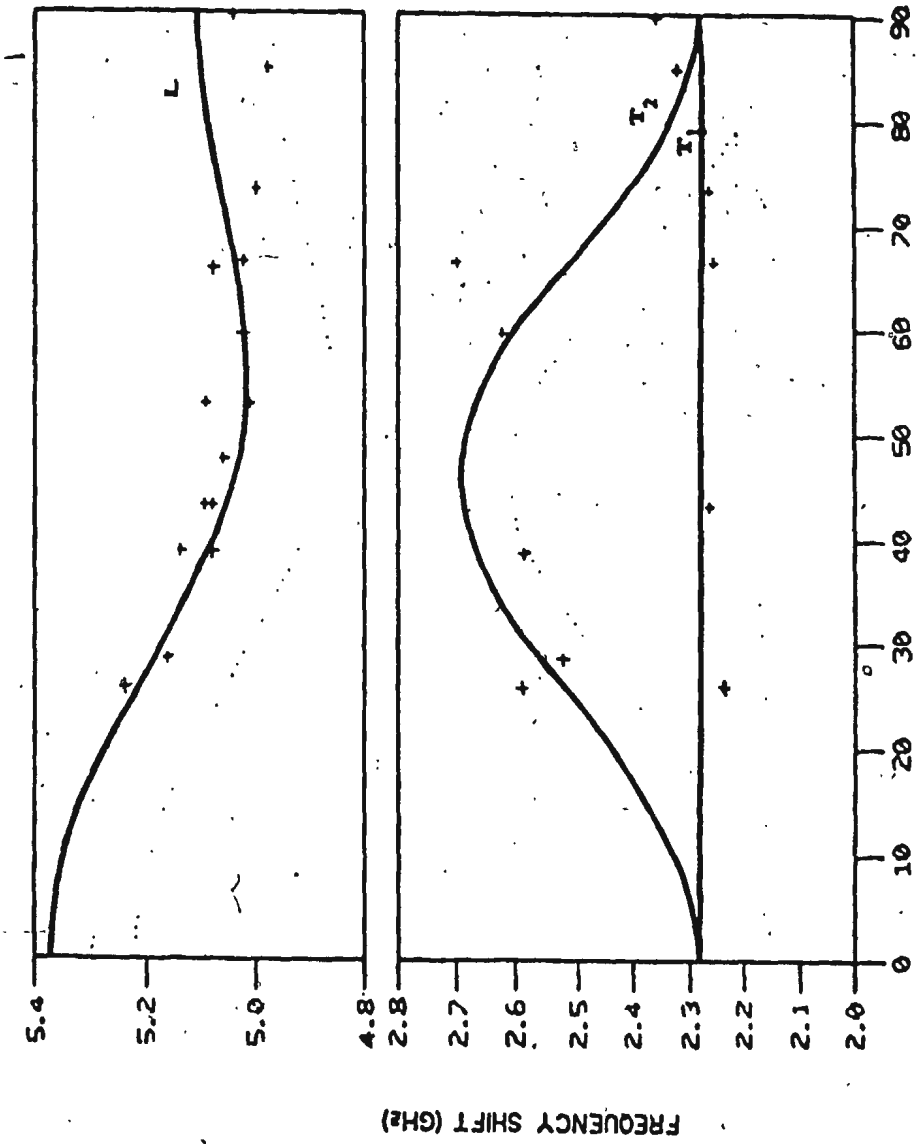
L
T_2
T_1
5.4
5.2
5.0
4.8
2.8
2.7
2.6
2.5
2.4
2.3
2.2
2.1
2.0
0
10
20
30
40
50
60
70
80
90
ANGLE GAMMA (DEGREES)
FREQUENCY SHIFT (GHz^2)

FIG. 3.2

standard deviation of the elastic constants. In addition, there is a systematic error due to the uncertainty in the values of the wavelength, index of refraction, density and the scattering angle. The wavelength was accurate to 1 in 10^4 and hence was treated as an exact parameter. The density and the refractive index had a percentage error of 1.3% and 1.9% respectively, as described above. The scattering angle had a percentage error of 0.55%. These errors add up to give a systematic error of 4.1% in the elastic constants.

These elastic constants can be compared to the values of the elastic constants at the triple point (35) which were also confirmed in this experiment:

c_{11}=1.909 c_{12}=1.151 c_{13}=0.955

c_{44}=0.356 c_{33}=2.104

We see that with decrease in temperature the crystal gets harder and the elastic constants increase. Fig.3.2 represents the variation of frequency shift with angle gamma. The solid and dotted curves are the best fit curves to the elastic constants at 62 K and 68 K respectively The 62 K curves are higher than the 68 K curves showing an increase in acoustic velocities with decrease in temperature.

b)β-N_2

Four single crystals of N_2 were cooled to 47.5 K giving 35 spectra at different crystal orientations (Table 3.2). Two of the sets of data, namely of crystals #1 and #2, are results obtained by S.F.Ahmad (at 49.0 K) which were temperature corrected to 47.5 K. The density of N_2 at 47.5 K was obtained in a similar manner to that of CO and was 0.976±0.015 gm/cm^3. The refractive index was also calculated using the

TABLE 3.2

Observed and calculated "best-fit" frequency shifts as a function of orientation for four N_2 single crystals at 47.5 K

Crystal #	Euler Angles θ	ϕ	χ	Observed Frequency Shift in GHz $\nu(L)$	$\nu(T_2)$	$\nu(T_1)$	Calculated Frequency Shift in GHz $\nu(L)$	$\nu(T_2)$	$\nu(T_1)$
$N_2$1	92.3	200.1	357.5	5.123	2.605	2.209	5.146	2.592	2.198
	92.1	183.7	358.5	5.133	-	2.198	5.160	2.588	2.190
	92.4	165.3	359.7	5.125	-	2.189	5.152	2.591	2.194
	92.7	145.4	360.0	5.113	2.537	2.213	5.136	2.569	2.211
	92.3	222.7	358.7	5.126	2.517	2.233	5.142	2.525	2.221
	92.0	241.7	359.0	5.223	-	-	5.191	2.344	2.243
	92.7	231.9	358.6	5.196	2.387	2.279	5.159	2.454	2.232
	92.3	212.1	359.3	5.115	2.568	2.225	5.136	2.575	2.209
	92.5	203.7	359.4	5.120	2.608	2.211	5.142	2.591	2.200
$N_2$2	25.1	184.9	180.8	5.207	-	2.271	5.197	2.326	2.245
	25.1	175.6	179.5	5.221	2.303	-	5.197	2.326	2.245
	25.5	168.1	178.3	5.194	2.316	-	5.197	2.325	2.245
	26.0	156.3	180.5	5.204	2.363	-	5.194	2.336	2.244
	25.3	149.2	178.6	5.196	2.320	-	5.185	2.364	2.242
	25.5	119.5	179.9	5.130	-	2.279	5.154	2.473	2.229

TABLE 3.2 continued

Crystal #	Euler Angles θ	φ	χ	Observed Frequency Shift in GHz ν(L)	ν(T₂)	ν(T₁)	Calculated Frequency Shift in GHz ν(L)	ν(T₂)	ν(T₁)
$N_2$3	118.0	268.1	18.2	5.202	2.342	-	5.193	2.337	2.244
	118.0	258.1	19.2	5.171	2.432	2.141	5.161	2.446	2.233
	118.0	258.1	19.2	5.139	2.536	-	5.161	2.446	2.233
	118.0	238.1	17.9	5.142	2.557	2.149	5.140	2.587	2.203
	118.0	238.1	17.9	5.143	2.551	-	5.140	2.587	2.203
	118.0	233.1	17.5	5.157	2.569	2.141	5.150	2.562	2.195
	118.0	228.1	17.3	5.143	2.578	-	5.168	2.582	2.187
	118.0	218.1	17.2	5.210	2.519	-	5.220	2.526	2.171
	118.0	213.1	17.3	5.231	2.492	2.144	5.251	2.484	2.164
	118.0	208.1	16.9	5.275	2.444	2.155	5.282	2.438	2.157
	118.0	208.1	16.9	5.214	2.538	-	5.282	2.438	2.157
	118.0	198.1	17.0	5.326	2.347	2.096	5.339	2.348	2.147
	118.0	188.1	17.2	5.381	-	2.175	5.375	2.285	2.141
$N_2$4	44.7	357.4	6.9	5.458	2.204	-	5.458	2.129	2.127
	44.7	347.4	6.8	5.446	2.161	-	5.438	2.169	2.130
	44.7	337.4	6.6	5.419	-	-	5.394	2.252	2.137
	44.7	327.4	6.0	5.368	2.356	-	5.333	2.357	2.148
	44.7	317.4	6.1	5.314	2.463	-	5.266	2.463	2.161
	44.7	307.4	6.3	5.258	2.560	-	5.204	2.545	2.175
	44.7	307.4	6.3	5.229	2.558	-	5.204	2.545	2.175

Fig. 3.3 The change in frequency shift with angle γ. The solid curve is a fit to the elastic constants of β-N_2 at 47.5 K. The dotted curve is a fit to the elastic constants at 63 K obtained by Kiefte and Clouter (9).

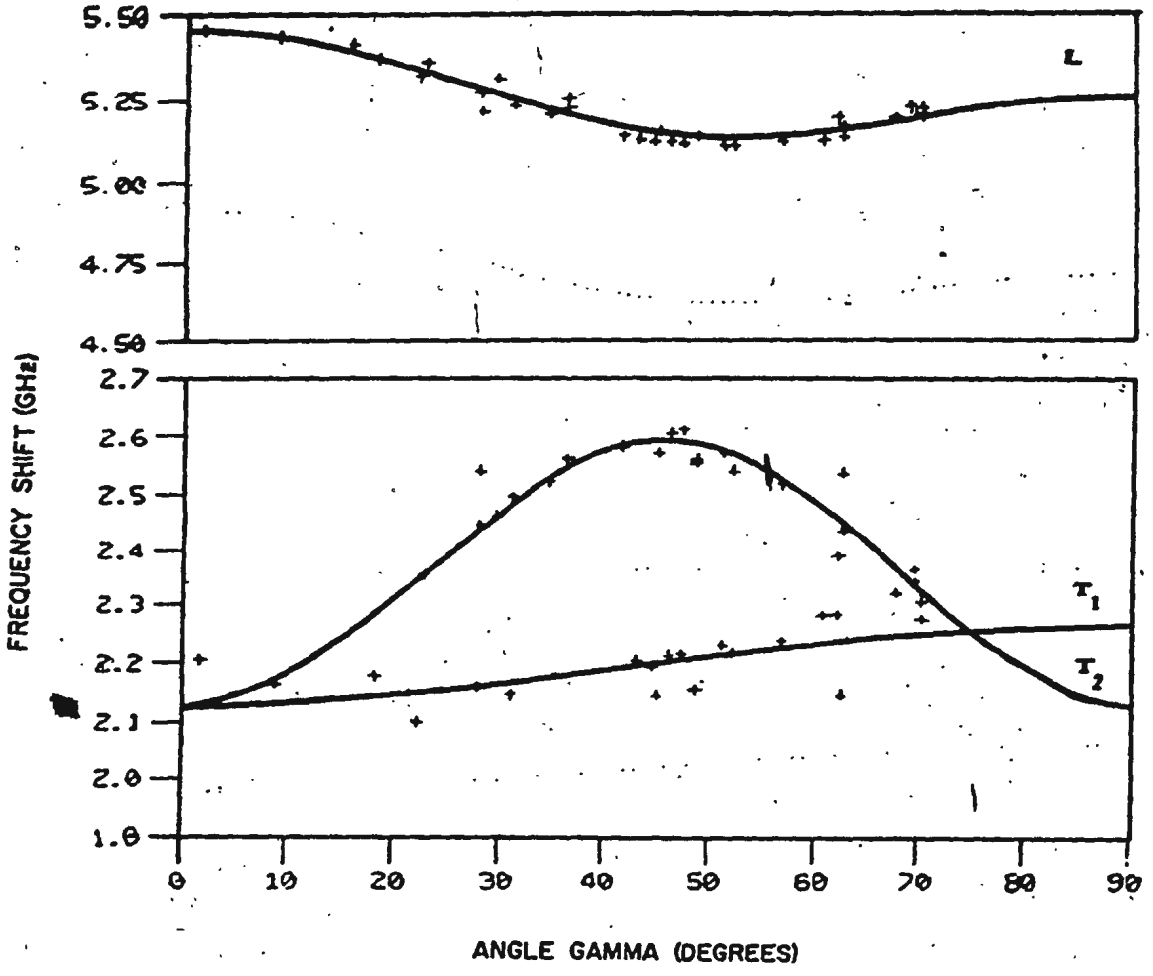
5.50
5.25
5.00
4.75
4.50
L
2.7
2.6
2.5
2.4
2.3
2.2
2.1
2.0
1.0
T_1
T_2
FREQUENCY SHIFT (GHz)
0
10
20
30
40
50
60
70
80
90
ANGLE GAMMA (DEGREES)

Fig. 3.3

density and refractive index at the triple point (9) and the Lorentz-Lorenz relation. The calculated value of refractive index for N_2 at 47.5 K was 1.244±0.007. The best-fit adiabatic elastic constants for N_2 in units of 10^9 N/m^2 are:

c_{11}=2.307±0.007 c_{12}=1.454±0.008 c_{13}=1.274±0.007

c_{44}=0.378±0.004 c_{33}=2.488±0.008

The adiabatic bulk modulus was calculated to be 1.678 in the same units.

The systematic errors involved in these measurements as noted above are: 1.5% error in density, 0.53% in refractive index and 0.55% in scattering angle. The overall systematic error is 2.04%. This error adds to the errors in the elastic constants.

These elastic constants can be compared to the values of elastic constants at the triple point (9):

c_{11}=1.825 c_{12}=1.131 c_{13}=0.980

c_{44}=0.320 c_{33}=1.976

Fig.3.3 shows the variation of frequency shift with gamma for N_2. The solid and dotted curves are best-fit curves to the elastic constants at 47.5 K and 63 K respectively. The 47.5 K curves are again higher than the 63 K curves and represent an increase in sound velocity with temperature decrease.

3-3 Phase Transformation

Several attempts were made to carry out the phase transition in N_2. However, it was not feasible to get lower than 47.5 K and maintain a good quality crystal for light scattering purposes. The main reason for this is that at these temperatures, the vapor pressure of N_2 is very

small (about 7 KPa). Hence pumping (and heating) does not have much affect on shaping the sample and freeing from the cell walls and in addition, if a dome-shape crystal is obtained it would not grow back to a suitable shape for light scattering purposes (again bacause of low vapor pressure).

Three large single crystals of f.c.c. α-CO were grown out of h.c.p. β-CO single crystals. By determining the orientation of each crystal relative to the laboratory frame of reference, it was possible to correlate the orientations of the two phases of CO.

The focus of all the calculations was the h.c.p. c-axis and hence the h.c.p. basal planes. Using the inverse rotation matrix (1.13)(with the Euler angles of the h.c.p. phase), the c-axis for each of the three β-CO crystals was transformed to the laboratory frame of reference. An application of the rotation matrix (inverse of A, eq. 1.13) with the Euler angles of the f.c.c. phase showed the new components for the c-axis in the f.c.c. structure. Calculations were further confirmed using styrofoam ball models of crystal structures of h.c.p. and f.c.c. set and rotated to their respective orientations in space.

Fig.3.4 shows a single crystal of the α phase growing from the bottom out of a single crystal of the β phase. The interface was fairly sharp and distinctly divided the crystal into an upper β phase and a lower α phase. The growth of the α phase is from the bottom because it is the low temperature part of the cell.

Just before the phase transition occured, the β phase underwent some dramatic changes. Bubble-like features appeared and the crystal became translucent. One might think that the crystal was no longer useful. However, after several hours the interface appeared. Although

Fig. 3.4 The growth of the α phase from the β phase. The horizontal line half way up in the cell is the boundary that visually separates the two phases.

the interface visually separated the two phases, x-ray diffraction patterns (Fig. 3.6b) indicated traces of the β phase left in the new α structure. Such behavior was also observed by Franck *et al.* (52) in the 50% completed h.c.p.-f.c.c. phase transition in He crystals and by Miller *et al.* (53) and Yarnell *et al.* (54) in the h.c.p. to f.c.c. transition in D_2. The complete transition occurred when the crystal was cooled further (0.1 to 0.3 K) and subsequent x-ray patterns indicated relatively pure cubic structure. Once the α phase was transformed, the crystal became wholly hexagonal having the same initial orientations. If cooled again through the phase transition, the crystal again became translucent and the cycle repeated. The f.c.c. structure generally had the same orientation as it had after the first attempt. These observations suggest that there is a definite correlation between the orientations of the two phases of CO.

Note that the following standard notation has been adopted (42):

( ), for a lattice plane

{ }, for a family of planes

[ ], for the direction of a lattice point

< >, for a family of directions

a)Crystal I

Fig.3.5a shows the Laue pattern of transmission x-ray diffraction for β-CO at 0° rotation of the cell. For the β phase, the orientation (i.e. the crystal body axes with respect to the laboratory frame of reference) was determined to be:

θ=110.4 ϕ=334.4 χ=104.6

These values agree with other patterns taken at 10° and 350° rotation

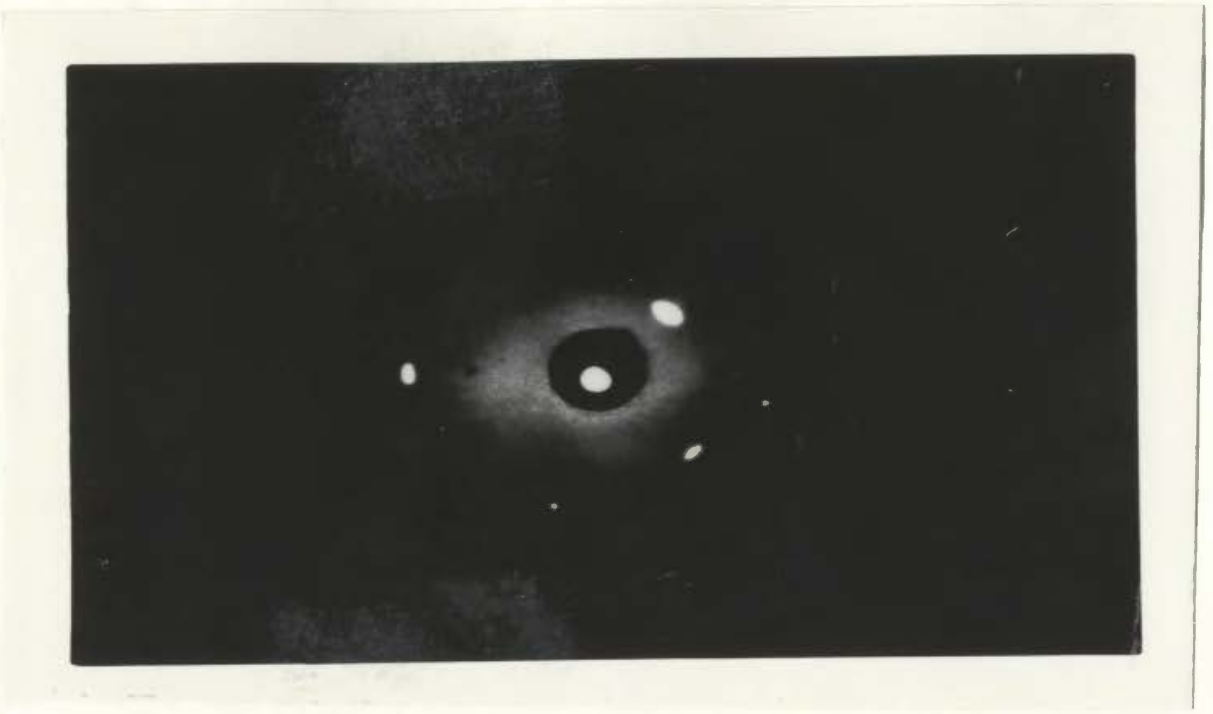

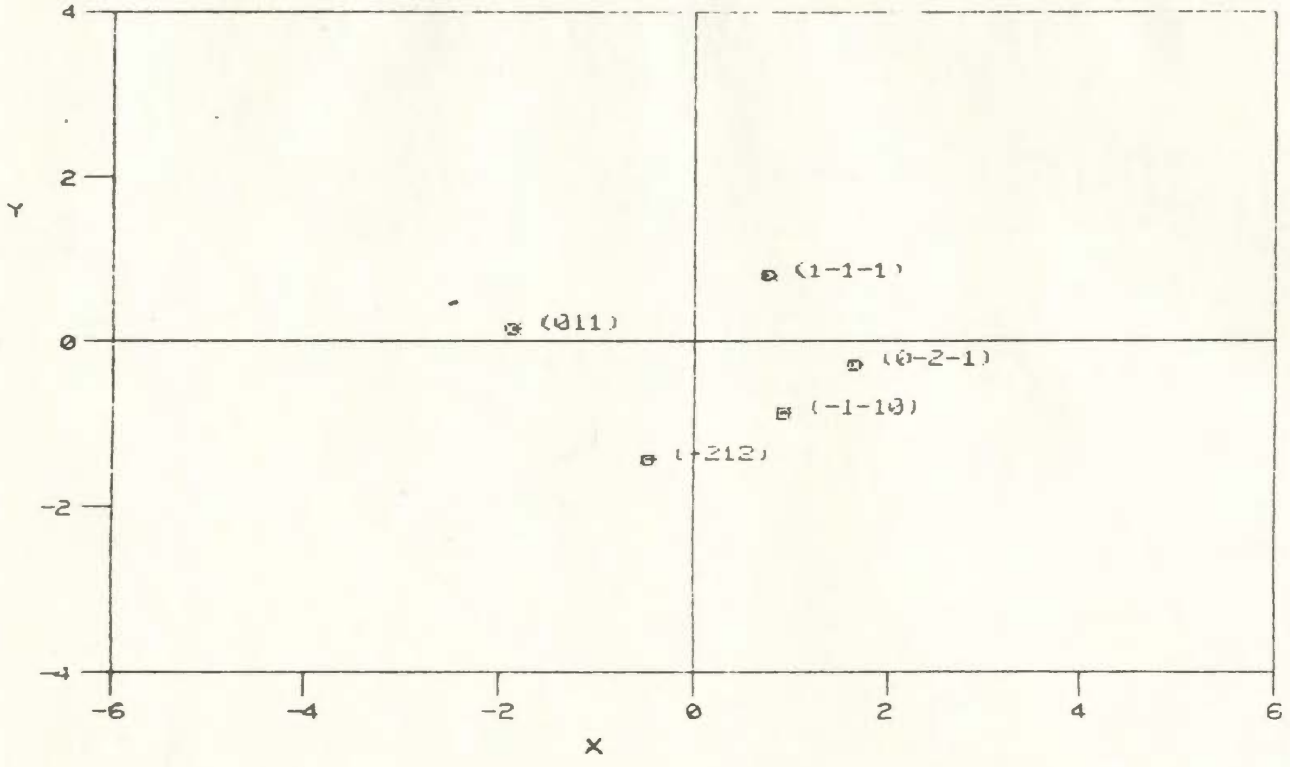

Fig. 3.5a The Laue diffraction pattern at 0° rotation of the cell of the β phase of crystal I. The Euler angles were (110.4,334.4,104.6).

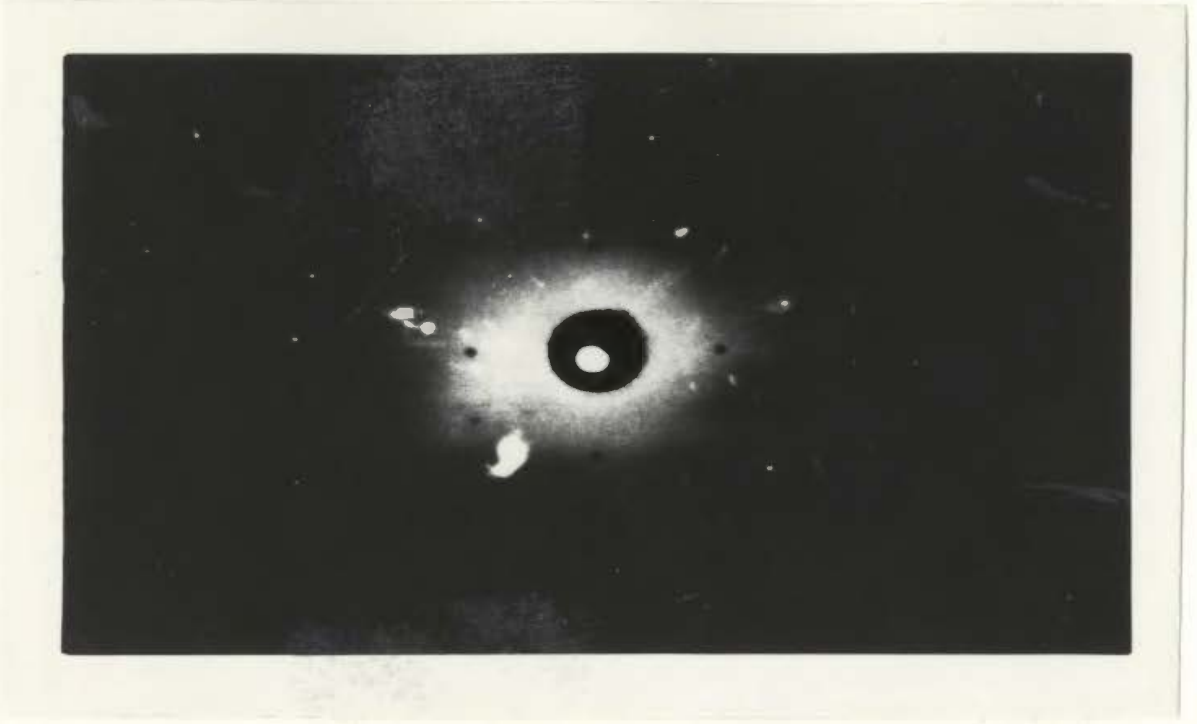

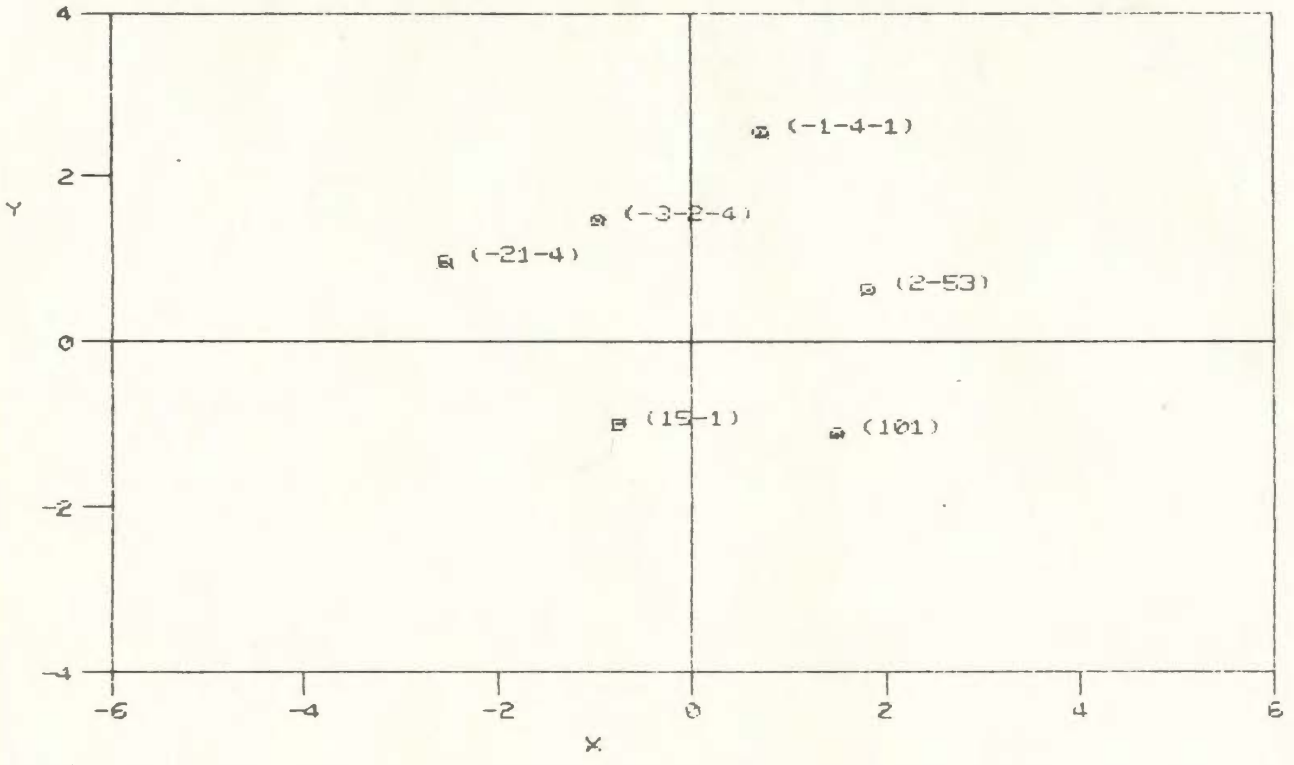

Fig. 3.5b The Laue diffraction pattern at 0° rotation of the cell of the α phase of crystal I. The Euler angles were (110.5,130.8,211.4).

of the cell. Fig.3.5b shows the orientation of the α phase for 0° rotation of the cell. The orientation obtained was:

θ=110.5 ϕ=130.8 χ=211.4

Using the transformation (1.13), the c-axis was calculated to have changed to $\begin{bmatrix} 0.64 \\ 0.33 \\ -0.68 \end{bmatrix}$ axis in the f.c.c. structure which is at an angle of 16° to the $[1\bar{1}\bar{1}]$ and 19° to the $[10\bar{1}]$ axes. This means that the h.c.p. basal plane is close to the $(10\bar{1})$ and $(11\bar{1})$ planes. The styrofoam ball models were used to confirm the calculations. The transition was somehow incomplete or at least the α crystal was not completely single. This is evident from Fig.3.5b since the spots are not as well defined as they should be. The α phase was "melted" and regrown again out of the β, however no further improvement was observed for this particular sample.

b)Crystal II

The orientation of the β phase (Fig.3.6a) was determined relative to the laboratory frame of reference and was found (at 0° rotation) to be:

θ=96.0 ϕ=128.7 χ=195.5

The phase transition was carried out and x-ray diffraction patterns were taken . The α phase was polycrystalline. As the interface between the two phases was lowered and the α phase "melted", the original β phase was recovered. Another attempt was made to cool the crystal through the transition temperature. This time the pictures (Fig.3.6c) consisted of more or less well defined spots. The orientation obtained

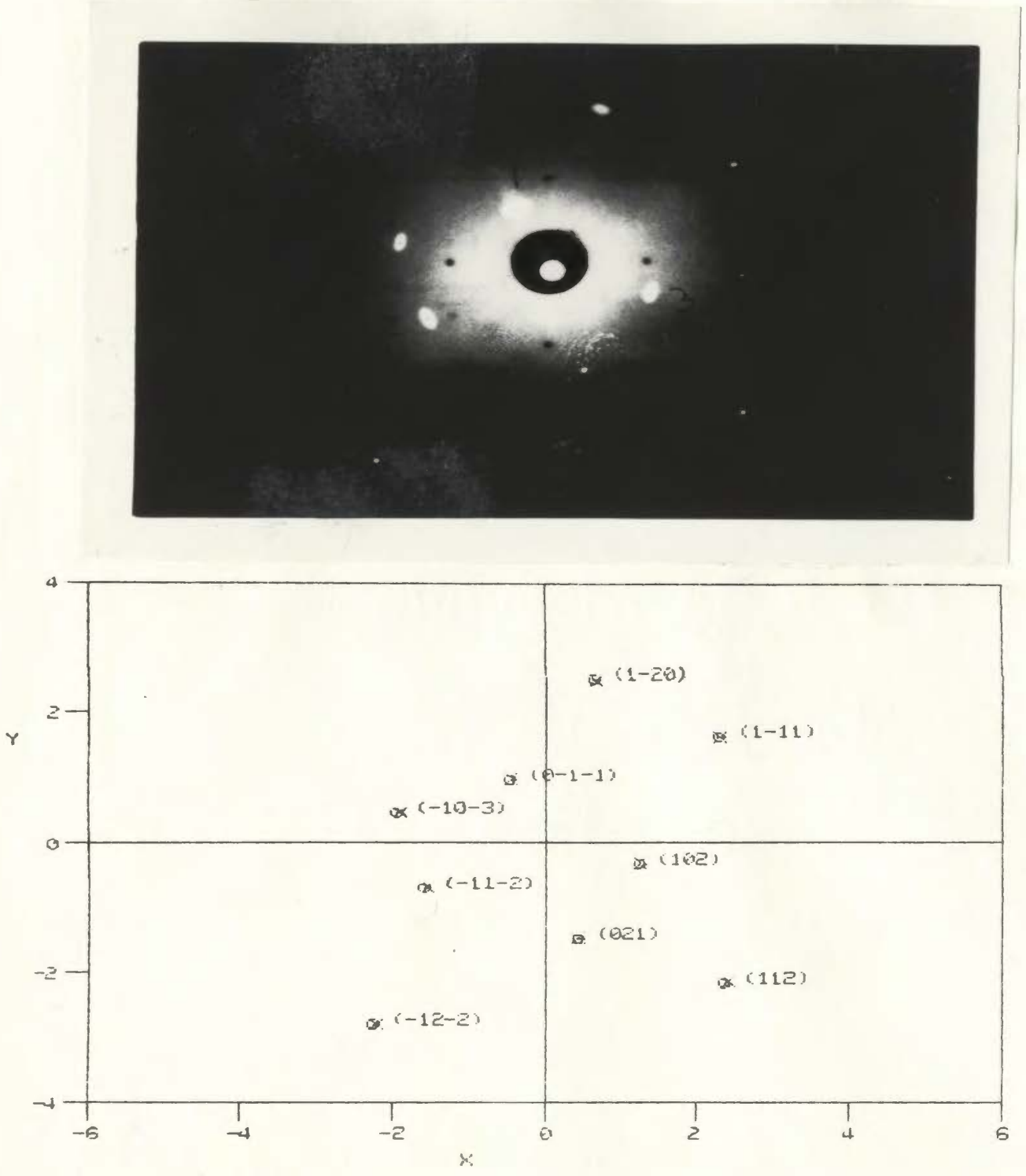

Fig. 3.6a The Laue diffraction pattern at 0° rotation of the cell of the β phase of crystal II. The Euler angles were (96.0,128.7,195.5).

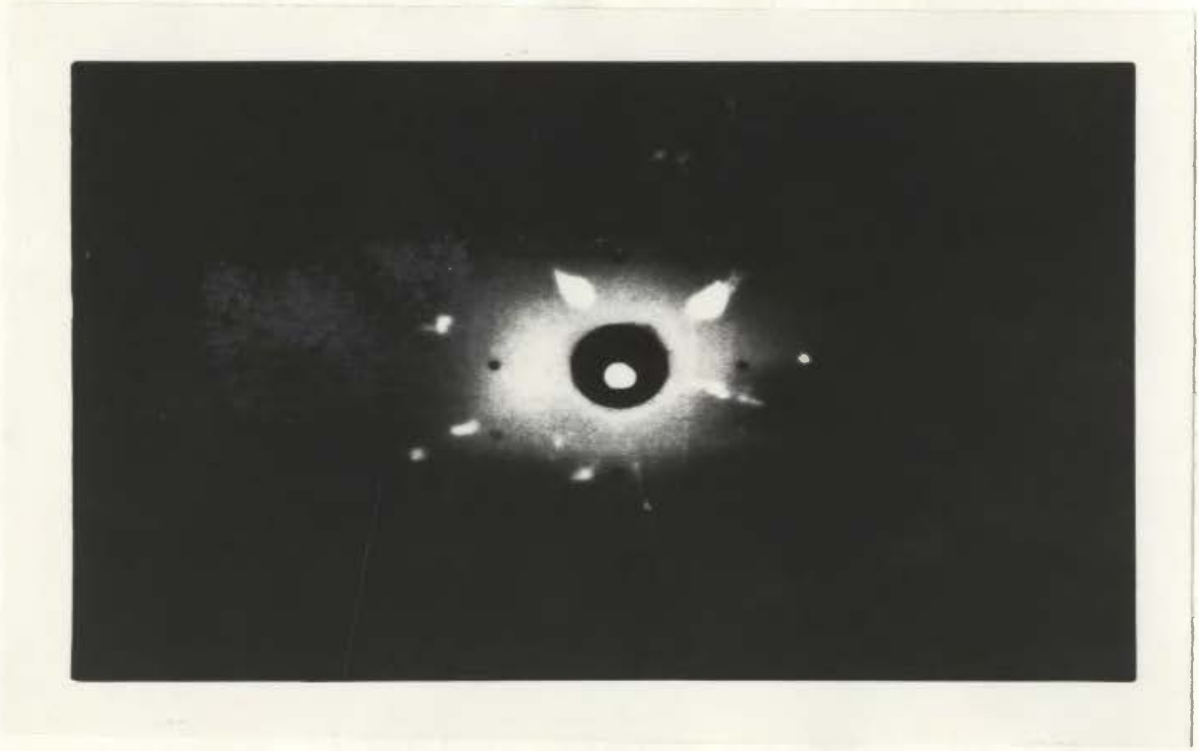

Fig. 3.6b The Laue diffraction pattern at 0° rotation of the cell shortly after the phase transition in crystal II.

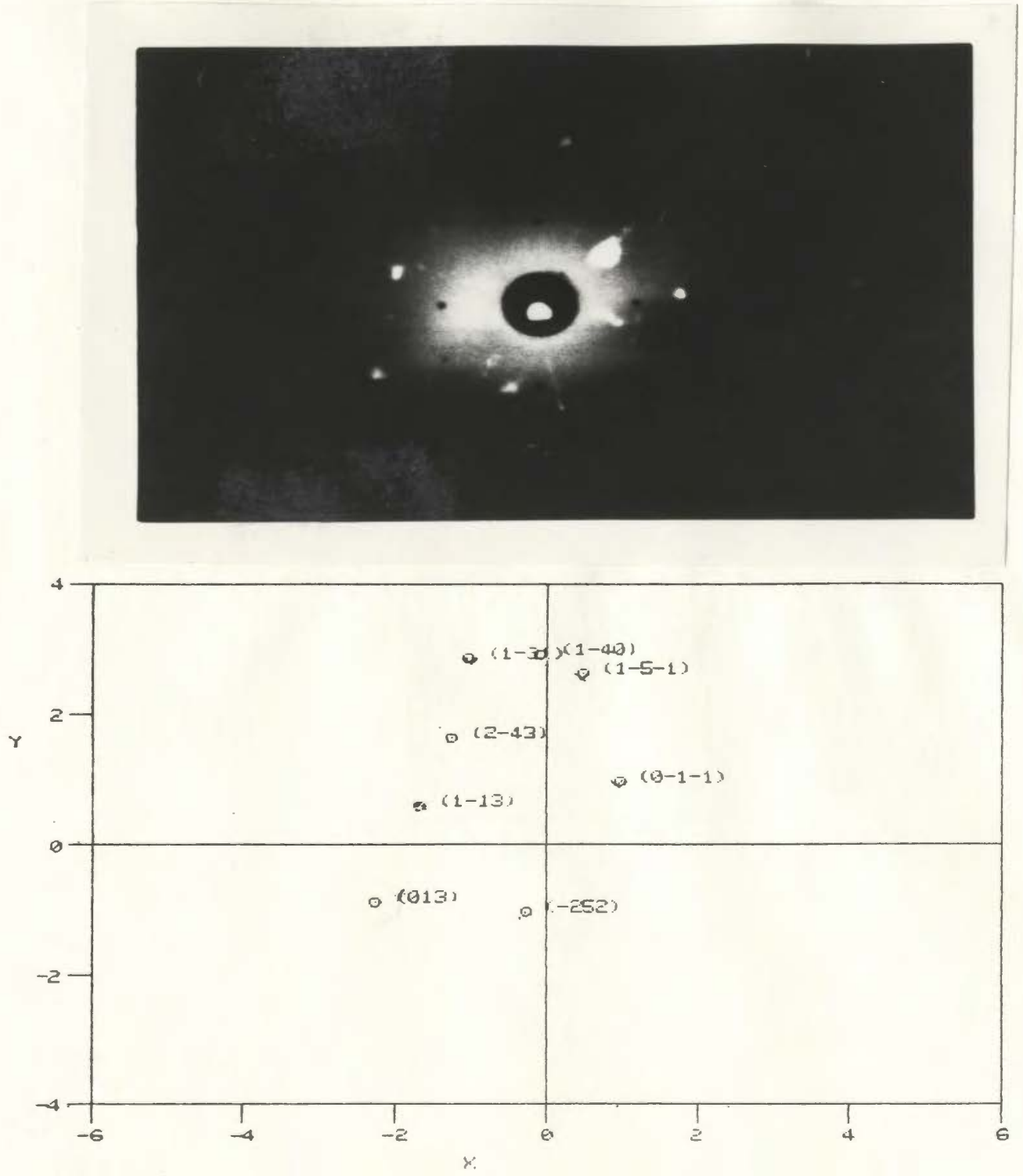

Fig. 3.6c The Laue diffraction pattern at 0° rotation of the cell of the α phase of crystal II. The Euler angles were (94.2,286.2,157.2).

was:

θ=94.2 ϕ=286.2 χ=157.2

This α phase was regrown twice through the β phase. Each time, the same orientation was obtained. The corresponding direction of the c-axis in the f.c.c. structure was found to be $\begin{bmatrix} 0.29 \\ 0.30 \\ -0.90 \end{bmatrix}$, which is about 30° to both $[01\bar{1}]$ and $[11\bar{1}]$ and 25° to $[00\bar{1}]$. The transition was again somewhat incomplete (or the α phase was not completely single).

c)Crystal III

As can be seen from Fig.3.7c, the transition was an excellent one in which well defined spots free of strain were observed. The orientations of the β phase (Fig.3.7a) were found to be:

θ=57.7 ϕ=32.6 χ=339.5

After the phase transition, the orientation was calculated and found to be:

θ=23.2 ϕ=273.9 χ=339.0

Using the inverse rotation matrices, the transformed c-axis in the f.c.c. structure was $\begin{bmatrix} 0.48 \\ 0.81 \\ 0.33 \end{bmatrix}$, which is within 19° of [111]. The next day, the crystal spontaneously had changed orientation and stayed stable afterwards with the following orientation:

θ=34.7 ϕ=170.6 χ=356.4

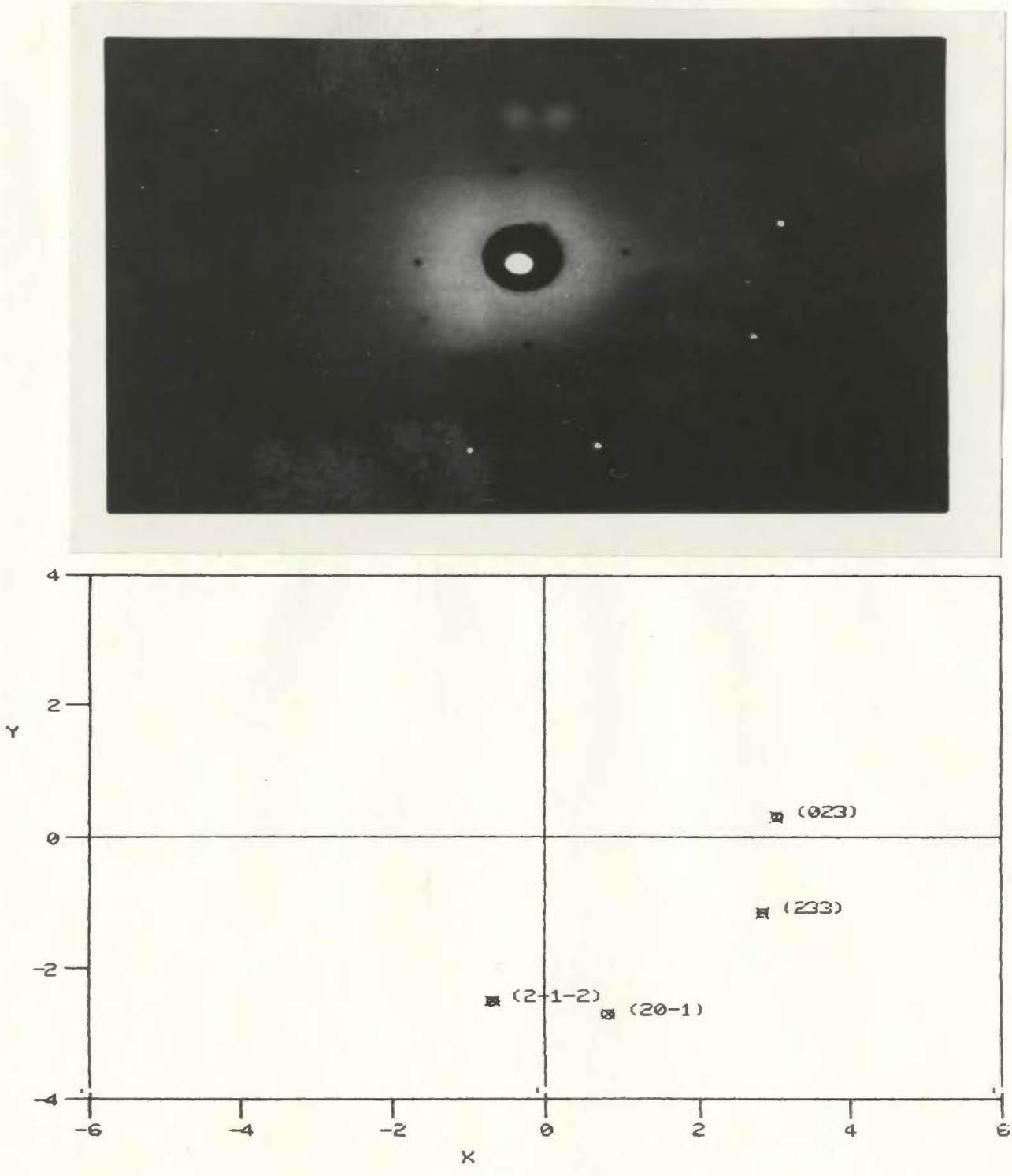

Fig. 3.7a The Laue diffraction pattern at 0° rotation of the cell of the β phase of crystal III. The Euler angles were (57.7,32.6,339.5).

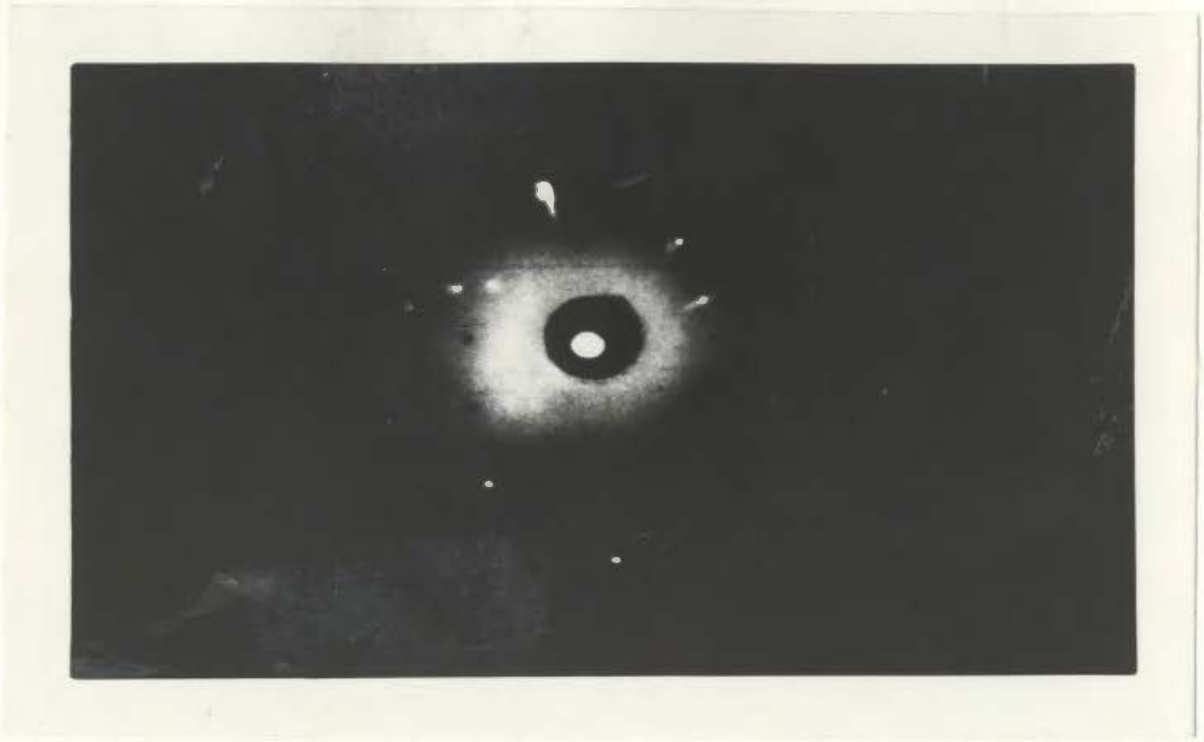

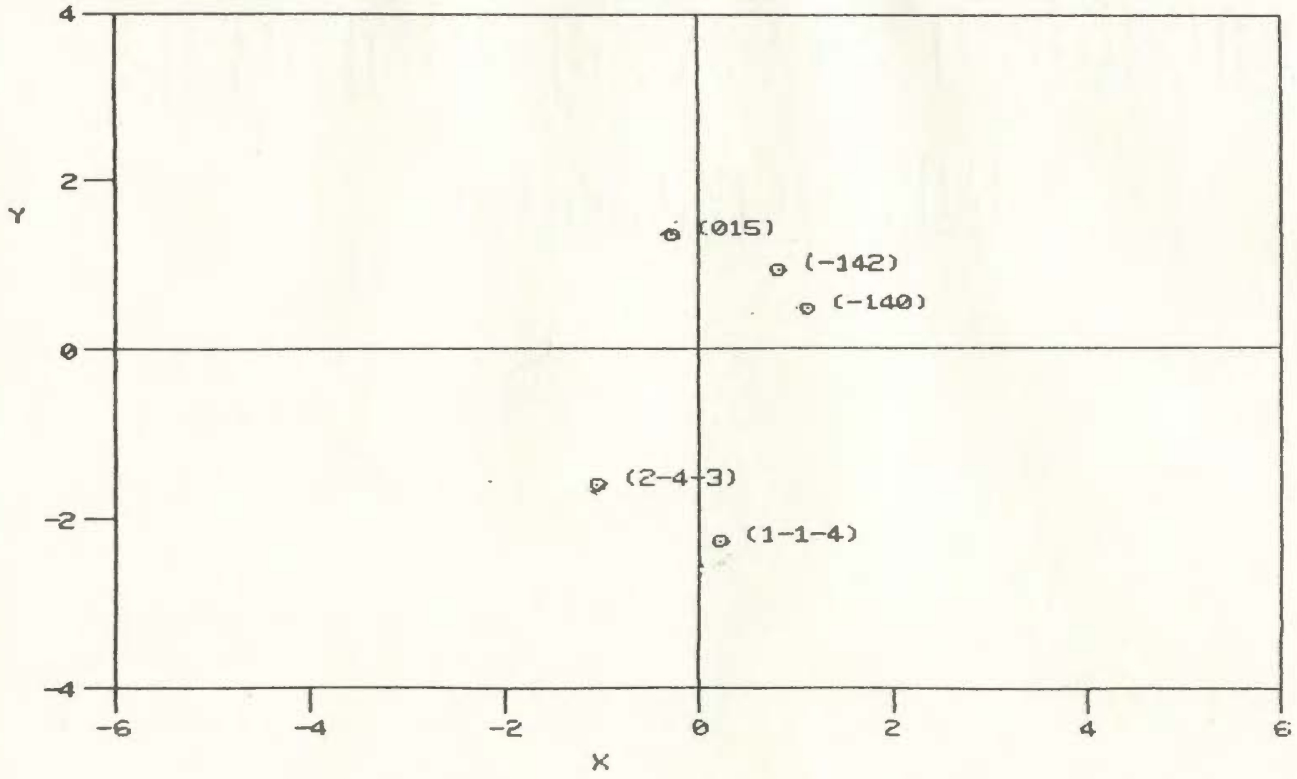

Fig. 3.7b The Laue diffraction pattern at 0° rotation of the cell of the initial α phase of crystal III. The Euler angles were (23.2,273.9,338.9).

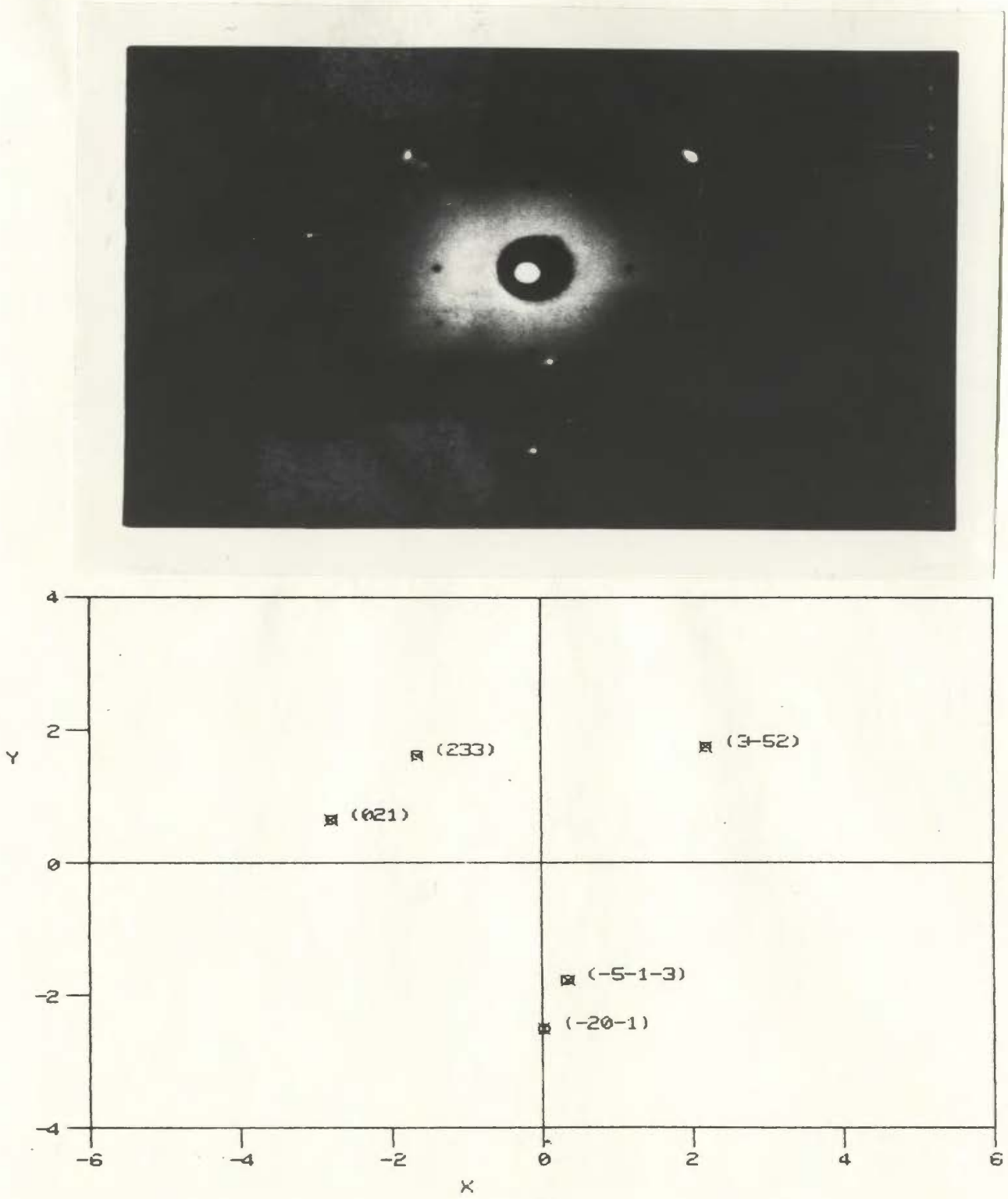

Fig. 3.7c The Laue diffraction pattern at 0° rotation of the cell of the final stable α phase of crystal III. The Euler angles were (34.7,170.6,356.4).

This orientation shows that the c-axis was transformed to $\begin{bmatrix} -0.60 \\ 0.70 \\ 0.09 \end{bmatrix}$, which almost exactly is the $[\bar{1}10]$ axis of the cubic phase. The spots this time were very well defined and the transition was clearly a very good one (i.e. appeared to be entirely single and very complete).

From crystal III (which involved the best and most clearly defined x-ray picture) it is clear that the final stable state for the h.c.p. basal planes were planes of the form { 110 } in preferance to { 111 }. This is consistent with crystals I and II where there appears to be competetion between { 111 } and { 110 } as shown above. On this basis (and for the lack of further clear evidence) it will be assumed and hence concluded for the rest of this thesis, that the basal planes of hexagonal close-packed structure transforms to planes of the form { 110 } in face centered cubic structure. It is interesting to note that Impey *et al.* (55) making molecular dynamics computer simulation calculations on different phases of solid ammonia determined that in the h.c.p. to b.c.c. phase transition , the h.c.p. basal planes become { 110 } planes of b.c.c. and is the least energetic way for the transition.

d)Mechanism Of Phase Transition In CO

There are various ways to imagine the mechanism of this transformation. One possibility is proposed here. Fig.3.8a shows the configuration of molecular sites for an h.c.p. crystal projected on the plane of the paper;

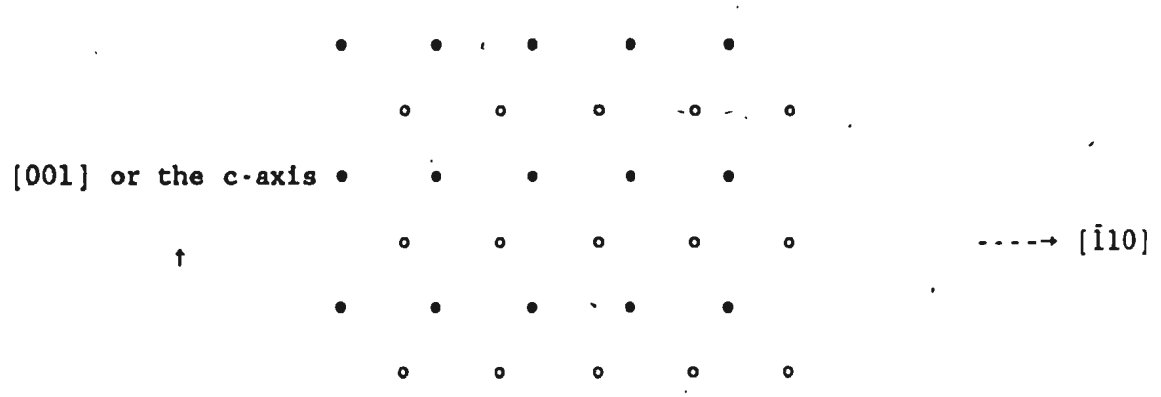

Fig.3.8a The h.c.p. crystal with c-axis up

where the solid circles represent one layer (A) and open circles the next layer (B), i.e. ABAB... stacking.

Note that the lattice vectors for h.c.p. are defined in terms of the cartesian coordinate system (body frame of reference) as:

$\mathbf{a} = \frac{\sqrt{3}}{2} a\hat{x} - \frac{1}{2} a\hat{y}$

$\mathbf{b} = a\hat{y}$

$\mathbf{c} = c\hat{z}$, where a and c are the lattice parameters of the hexagonal crystal. The direction of the x-axis is then [210] and the y-axis is [010] in terms of the lattice vectors.

Looking along the c-axis, we see the following (Fig.3.8b);

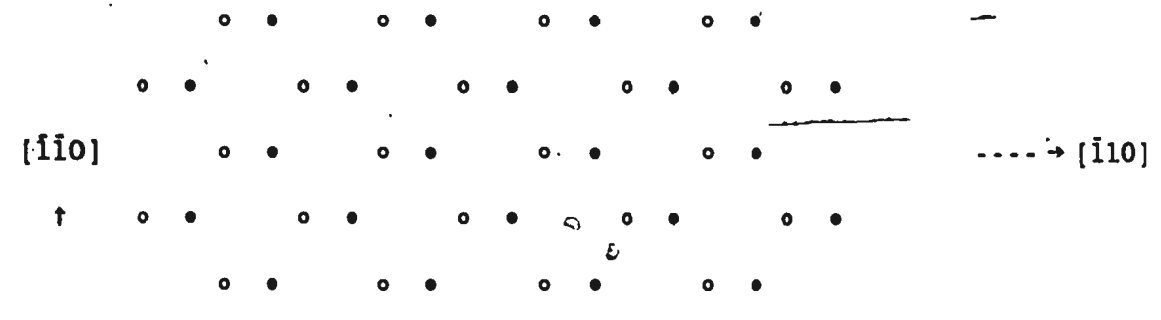

Fig.3.8b The h.c.p. crystal looking along the c-axis

The alternate planes then start moving relative to one another and in so doing the c-axis of the h.c.p. may end up in the [111] direction of the cubic as happened in crystal III and as is generally theoretically expected. This will not (and apparently did not) stay long and the relative movement continues until the arrangement in fig.3.8b becomes as shown below (from Fig.3.8b, it requires a shearing movement of the alternate basal planes by $a/2\sqrt{6}$ in the $[\bar{1}10]$ direction where a is the side of cube in the f.c.c. structure);

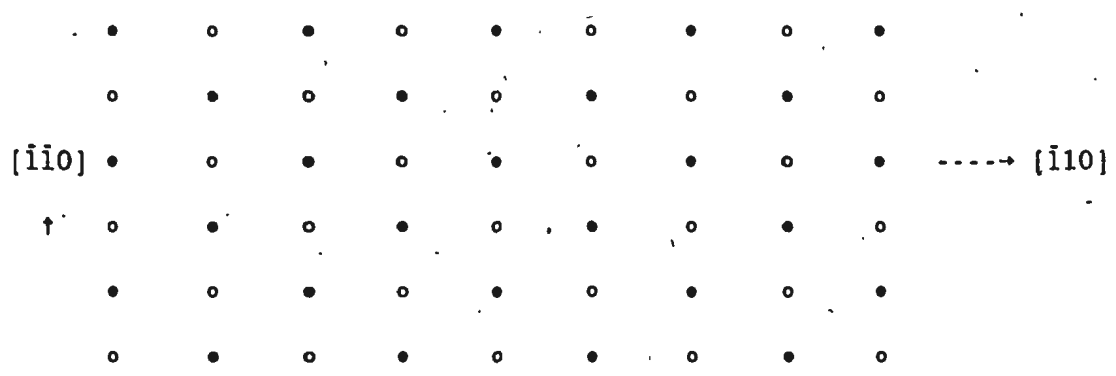

Fig.3.8c The same crystal with alternate planes moved as discussed in text.

Now the distance between two successive circles (open or closed) is $3a/\sqrt{6}$ where a is the side of cube. If in 7 planes the first and last planes are considered to remain stationary and the second plane is moved to the right by $a/2\sqrt{6}$, the third plane to the right by $a/\sqrt{6}$, the fourth plane to the right by $3a/2\sqrt{6}$, the fifth plane to the left by $a/\sqrt{6}$ and the sixth plane to the left by $a/2\sqrt{6}$ relative to the first and last planes in $[\bar{1}10]$ direction, the result is as shown below;

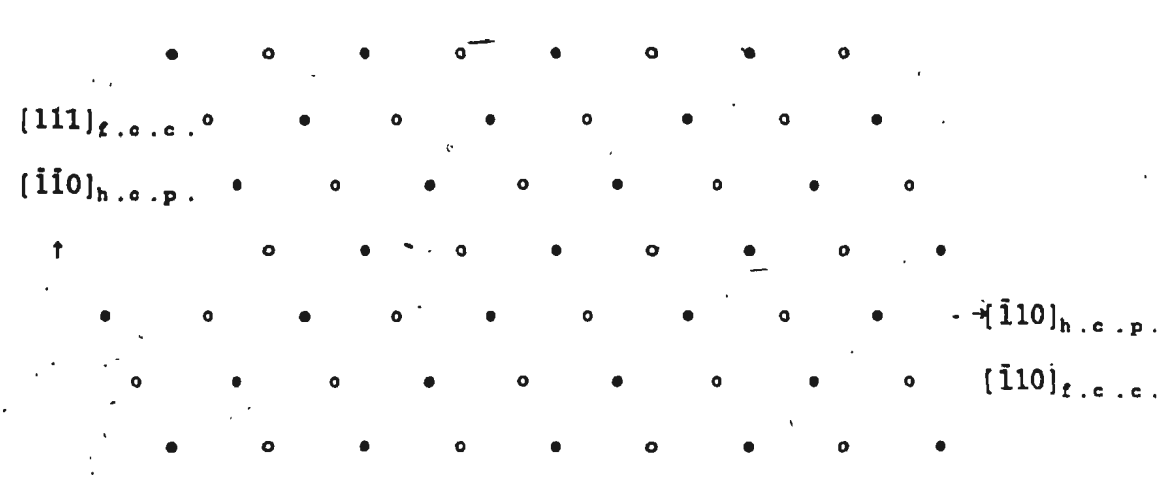

Fig.3.8d The basal planes after the shearing movements

Fig.3.8.d has the same arrangements as that of the planes of the form { 110 } in the f.c.c. structure with the cubic [111] axis up in the plane of paper (note the ABCABC... stacking). The relative shearing movement is a/2√6.

CHAPTER 4

DISCUSSION

4-1 Elastic Constants

Goldman and Klein (21), used the self-consistent phonon approximation of anharmonic lattice dynamics to calculate the elastic constants of h.c.p. nitrogen via a (12-6) Lennard-Jones intermolecular potential and assuming disordered molecular orientations. The values of elastic constants calculated at 63 K were: c_{11}=2.88, c_{12}=1.09, c_{13}=0.88, c_{44}=0.65 and c_{33}=3.11 (see Table 4.1). These theoretical values are much larger (eg. c_{44} is twice larger) than the experimental values obtained by Kiefte and Clouter (9) showing the inadequacy of the theory and which is probably due in part to neglect of rotation-translation coupling effect. Kjems and Dolling (24) used the technique of inelastic neutron scattering to determine the translational and librational lattice modes in a single crystal of f.c.c. nitrogen at 15 K. By measuring the dispersion curves for certain acoustic modes, the three elastic constants could be deduced from the initial slopes of these curves and were found to be c_{11}=2.90, c_{12}=2.00 and c_{44}=1.35. They have also measured the three elastic constants of β-nitrogen at 37 K using the same technique (20) and they are: c_{11}=2.55, c_{33}=2.71 and c_{44}=0.43 (see Table 4.1). This represents reasonable agreement with the present 47.5 K results when extrapolated to 37 K. Powell *et al.* (19) used this technique to determine the three elastic constants of β-N_2 at 55 K and 400 MPa. The values for high pressure elastic constants are: c_{11}=4.43, c_{33}=5.92 and c_{44}=0.61. As is evident, the elastic constants

TABLE 4.1

Elastic Constants of N_2 and CO at different temperatures. The data for N_2 at 37 K have been obtained from neutron scattering experiments.

Elastic Constants (10^9 N/m^2)	N_2			CO	
	63K	47.5K	37K (neutron)	68K	62K
c_{11}	1.825	2.307	2.55	1.909	2.013
c_{12}	1.131	1.454	-	1.151	1.212
c_{13}	0.98	1.274	-	0.955	0.998
c_{44}	0.32	0.378	0.43	0.356	0.402
c_{33}	1.976	2.488	2.71	2.104	2.227

appear to increase dramatically with pressure. Mention should also be made of Bezuglyi *et al.* (56) work on determination of sound velocity in nitrogen using ultrasonic technique from 16 to 56 K. They determined the adiabatic bulk modulus of N_2 at 48 K to be 1.32 (in 10^9 N/m^2) which does not agree with the value of 1.67 obtained in the present work at 47.5 K.

The experimental values of elastic constants of cooled single crystals of N_2 and CO were seen to be larger than the ones for uncooled crystals (they all increased by about 1% / K. There appears to be no real evidence for mode softening as reflected in any one of the elastic constants. It was suggested by Page (1) that martensitic phase changes in AuCd, InTl and TiNi are preceded by softening of certain elastic constants and the transition results from the lattice instability evidenced as a soft acoustic mode. He suggested that as the incipient mechanical instability rises, certain modes undergo considerable energy decrease and as their frequency falls, the wavelength increases and the interatomic binding forces are decreased. Eventually the vibration amplitude and anharmonicity will be so large that the atoms adopt new sites. Although the phase transition in CO is martensitic, no significant mode softening was evident within a degree above the phase transition temperature.

4-2 The α-β Phase Transition

A cooled single crystal study has been done on nitrogen by Powell *et al.* (19) on elastic and inelastic neutron scattering measurements at 55 K and 400 MPa pressure. A single crystal of β-N_2 was grown by slow cooling under high pressure (700 MPa) and 150 K. The high temperature

crystal was cooled steadily at 10 K per day to 55 K and 400 MPa.

Several people have obtained single crystals of α-N_2. Cromer *et al.* (57) spent two months working at room temperature and 4.9 GPa pressure and obtained low strain single f.c.c. nitrogen crystal through an annealing process. Streib *et al.* (14) grew over 20 single crystals of β-N_2 and cooled each one carefully through the transition point but only once they obtained a single crystal of α-N_2. Kjems and Dolling (24), by cooling the β-N_2 crystals slowly, obtained a single crystal of α nitrogen of 1.5 cm^3 in volume surrounded by many small disoriented fragments and apparently were able to correlate the α and β phases. The orientation of the large crystal was consistent with that of the initial β phase crystal: the [111] and [0$\bar{1}$1] cube axes being parallel to the initial [001] and [110] hexagonal axes.

The transformation from h.c.p. to f.c.c. in CO appears to be a martensitic transformation. As noted by Christian (46), there are several characteristics of these transformations that were observed in the transition of CO. The transformation was time independent. In other words, the sample could be left for long times with the interface separating two phases and only a temperature change would affect the height of the interface. The other aspect of this transformation was its reversibility. The interface between the phases could be lowered and made to vanish by increasing the temperature, the resulting h.c.p. crystal having the same orientation as that of the parent h.c.p. crystal as noted before. The volume change involved is very little. Most importantly, there seems to exist a definite relation between the orientations of the original structure and that of the new phase.

Metallurgists have studied several f.c.c. to h.c.p. phase

transitions in metals and alloys. Laird and Aaronson (58) studied the isothermal formation of the h.c.p. phase from a supersaturated f.c.c. phase in Al-15 AtWt% Ag. They were able to establish the following relations between the planes and directions of the phases:

$(111)_{f.c.c.} \parallel (001)_{h.c.p.}$ and $[1\bar{1}0]_{f.c.c.} \parallel [100]_{h.c.p.}$

The transformation is supposed to be a martensitic type of surface relief. Kotval and Honeycombe (59) investigated the f.c.c. to h.c.p. phase transformation in CuGe alloys 12.5 Wt% Ge and CuGe 10 Wt% Ge alloys. The transition occurs both by stress inducement and thermal activation from a supersaturated f.c.c. phase and they claimed that both transformations are martensitic. In Cu-12.5Ge, the habit plane was {111} and the relation among planes and directions is similar to the Al-Ag work. The interface plane $(111)_{f.c.c.} \parallel (001)_{h.c.p.}$ has the same atomic configuration in both phases perhaps resulting in a coherency effect. Christian (60) studied this kind of transformation in pure cobalt and showed that the transformation is martensitic and that the f.c.c. (111) plane is parallel to the h.c.p. (001) plane and that the f.c.c. $[1\bar{1}0]$ direction is parallel to the h.c.p. [110] direction. A simple shear in the $[11\bar{2}]$ direction will carry out the transformation if every two planes are locked together. Thus the atoms in first, third and fifth planes shear on one another. The displacement is $a/\sqrt{6}$, where a is the side of cube and the shearing angle is 19°. Dislocations are assumed to be responsible for the transformation. Cobalt alloys(61) undergo a similar transformation from f.c.c. to h.c.p.. The orientation relations are: $(111)_{f.c.c.} \parallel (001)_{h.c.p.}$ and $[11\bar{2}]_{f.c.c.} \parallel [1\bar{1}0]_{h.c.p.}$ and is called the Shoji-Nishiyama relation. The shear angle is 19.5°. It is evident that there are inconsistencies in the metallurgy work.

In comparison with metals it must be noted that the type of binding in metals is stronger than the atomic interaction in crystals such as CO. The CO crystal is very soft and has low elastic constants mainly due to Van der Waals interaction type. Little work has been done on molecular crystals because of the difficulty in cooling large single crystals (as noted before) and maintaining it during and after the transition. J.P. Franck *et al.* (62,63) has done extensive research on the h.c.p. to f.c.c. phase transition in He especially in the vicinity of the triple point. He observed that the transition starts at a certain temperature and completes only over a finite temperature interval. At each point in this interval, the transition takes place at high speed, but only a fraction of the crystal transforms. The c-axis orientation is found to be reproducible as far as prolonged annealing is avoided. He thus claimed that the transition is of martensitic type.

Schuch *et al.* (64) studied the h.c.p.-f.c.c. structure change in H_2 and D_2 using x-ray diffraction technique. Although in their work the hydrogen isotope solidified in a mass of crystallites, there was a noticable preference for the orientation of the c-axis perpendicular to the cold cell wall. They measured the intensity of x-ray reflection, characteristic of either hexagonal or cubic. They suggested that changes occur by a simple sliding of hexagonal nets relative to one another. They noticed that no intensity change took place when the hexagonal { 002 } reflection became the { 111 } reflection in cubic. The spacings between the planes remained unchanged. However, in one experiment the transition was observed through a unique { 111 } cubic reflection which did not transform to { 002 } hexagonal reflection. The neutron studies by Yarnell *et al.* (53) showed that the nature of the

h.c.p.- f.c.c. transition in H_2 and D_2 is martensitic and they suggested a substantial density of stacking faults of hexagonal planes evidenced by shifts and widths of the elastic neutron lines in both phases. In the f.c.c. structure the perfect crystal is ABCABC, faults of ABCABABC or ABCABCBACBAC can occur. In h.c.p. the perfect crystal is ABABAB along the c-axis. Faults of ABABCACA or ABABCBCB can occur. Hardy *et al.* (65) used Raman scattering studies on solid H_2 and D_2 in which the [111] direction of crystallites was oriented along incident light beam. The latter configuration was considered because of evidence that the c-axis of hexagonal phase orients along the direction of crystal growth. Using the intensity measurements they suggested that the h.c.p. to f.c.c. transition takes place by shifting of hexagonal planes and the c-axis becomes the cubic body diagonal (111) axis.

Silvera (66) however mentioned that in a H_2 crystal there is a large potential barrier for such a shifting motion and at the low temperature of phase transition the thermodynamic probability for such a motion is extremely small. The energy gained per molecule by orientational ordering is of the order of T_c ~ 3-4 K whereas the barrier is at least of the order of melting temperature (15-20 K) per molecule and hence the ordering will not be able to drive the planes over the barrier. He further suggested that the transition probably takes place by motion of faults so that the barrier does not have to be crossed.

Other related work, although not the h.c.p.-f.c.c. transition is a paper on oxygen and its various phases. Defotis (67) studied the Laue diffraction pattern of single cubic γ phase and preferentially oriented polycrystalline rhombohedral β and monoclinic α oxygen. He established

the relations between the planes in the γ-β' and β-α transitions. However, the α and β crystals were not single and there is no h.c.p.-f.c.c. transformation involved. He observed that the exact relationship among the three modifications of alpha oxygen is not precisely that predicted by theory. This is also the case in the present work .

In the present experiment there are possibly competing factors that contributed to the incomplete phase transition in crystals I and II and to the lack of agreement with simple theoretical models. In addition, of course to the orientation of the parent crystal at the top from which the daughter phase is initiated, the walls of the cell are boundary conditions imposing constraints on the transition. The possible presence of tiny particles or sharp edges at the bottom of the cell (as a nucleation site) also influences the growth of the daughter phase. These factors could be the reason why the transition relationships are not definite for crystals I and II in that there appears to be competition between formation of planes of the form { 111 } and { 110 } (in the f.c.c. phase) on transition from { 001 } (in the h.c.p. phase). Crystal III did not stay in the { 111 } f.c.c. configuration and spontaneously changed to { 110 } [redacted]figuration. Theoretical understanding of the f.c.c.-h.c.p. phase transition in these very simple molecular solids is still clearly not satisfactory.

REFERENCES

1. N. G. Page and G. A. Saunders. Nat. Phys. Sci. 237, 47 (1972).
2. R. C. Weast, S. M. Selby and C. D. Hodgman. Handbook Of Chemistry and Physics. The Chemical Rubber Co., Cleveland, Ohio. (1964).
3. J. Timmermans. Physico-Chemical Constants Of Pure Organic Compounds, Elsevier, New York. (1950).
4. T. A. Scott. Phys. Rep. 27, 89 (1976).
5. W. Frels, D. R. Smith and T. Ashworth. Cryogenics 14, 3 (1974).
6. W. J. Briels, A. P. J. Jansen and A. van der Avoird. J. de Chim. Phys. 82, 125 (1985).
7. C. S. Barrett and L. Meyer. J. Chem. Phys. 43, 3502 (1965).
8. J. C. Raich and R. L. Mills. J. Chem. Phys. 55, 1811 (1971).
9. H. Kiefte and M. J. Clouter. J. Chem. Phys. 64, 1816 (1976).
10. P. H. Gammon. M.Sc. Thesis. Memorial University of Newfoundland, St. John's. 1978.
11. E. Fukushima, A. A. V. Gibson and T. A. Scott. J. Low Temp. Phys. 28, 157 (1977).
12. V. V. Nauchitel' and I. B. Golovanov. Sov. Phys. Cryst. 30, 27 (1985).
13. R. L. Mills. B. Olinger and D. T. Cromer. J. Chem. Phys. 84, 2837 (1968).
14. W. E. Streib, T. H. Jordan, H. W. Smith and W. N. Lipscomb. J. Chem. Phys. 41, 756 (1964).
15. R. L. Mills, D. Schiferl, D. T. Cromer, R. R. Ryan, A. C. Larson and R. LeSar. Acta Cryst. C, 39, 1151 (1983).

16. L. H. Bolz, M. E. Boyd, F. A. Mauer and H. S. Peiser. Acta Cryst. 12, 247 (1959).

17. D. J. Gannon and J. A. Morrison. Can. J. Phys. 51, 1590 (1973).

18. M. L. Klein and J. J. Weiss. J. Chem. Phys. 67, 217 (1977).

19. B. M. Powell, G. Dolling and H. F. Nieman. J. Chem. Phys. 79, 982 (1983).

20. J. K. Kjems and G. Dolling. In Reference 19, p.988.

21. V. V. Goldman and M. L. Klein. J. Chem. Phys. 64, 5121 (1976).

22. J. A. Venables and C. A. English. Acta Cryst. B, 30, 929 (1974).

23. E. M. Horl and L. Morton. Acta Cryst, 14, 11 (1961).

24. J. K. Kjems and G. Dolling. Phys. Rev. B, 11, 1639 (1975).

25. J. A. Venables. Phil. Mag. 21, 147 (1970).

26. M. M. Thiery, D. Fabre, M. Jean-Louis and H. Vu. J. Chem. Phys. 59, 4559 (1973).

27. A. Anderson, T. S. Sun and M. C. A. Dunkersloot. Can. J. Phys. 48, 2265 (1970).

28. M. M. Thiery and V. Chandrasekharan. J. Chem. Phys. 67, 3659 (1977).

29. J. J. Weiss and M. L. Klein. J. Chem. Phys. 63, 2869 (1975).

30. C. A. Swenson. J. Chem. Phys. 23, 1963 (1955).

31. R. L. Mills, D. H. Liebenberg and J. C. Bronson. J. Chem. Phys. 63, 4026 (1975).

32. S. Buchsbaum, R. L. Mills and D. Schiferl. J. Phys. Chem. 88, 2522 (1984).

33. R. LeSar and R. G. Gordon. J. Chem. Phys. 78, 4991 (1983).

34. D. Schiferl, D. T. Cromer, R. LeSar and R. L. Mills. Acta Crystallogr. C, 39, 1146 (1983).

35. P. H. Gammon, H. Kiefte and M. J. Clouter. J. Chem. Phys. 70, 810 (1979).

36. R. Stevenson. J. Chem. Phys. 27, 673 (1957).

37. A. I. Katz, D. Schiferl and R. L. Mills. J. Phys. Chem. 88, 3176 (1984).

38. E. K. Gill and J. A. Morrison. J. Chem. Phys. 45, 1585 (1966).

39. E. Fukushima, A. A. V. Gibson and T. A. Scott. J. Chem. Phys. 66, 4811 (1977).

40. B. P. Stoicheff. Chapter 16, Rare Gas Solids, Vol. II. Editors M. L. Klein and J. A. Venebles. Academic Press, London. 1976.

41. W. Hayes and R. Loudon. Scattering Of Light By Crystals. John Wiley & Sons, Inc., New York, 1978.

42. N. W. Ashcroft and N. D. Mermin. Solid State Physics, Holt, Rinehart and Winston, New York, 1976. P. 481.

43. L. D. Landau and E. M. Lifshitz. Theory Of Elasticity. Addison-Wesley Pub. Com., Inc., Massachusetts, 1959.

44. M. J. P. Musgrave. Crystal Acoustics. Holden Day, Inc., San Franscisco, 1970.

45. H. Goldstein. Classical Mechanics. Addison-Wesley Pub. Co., Inc., Massachusetts, 1959.

46. J. W. Christian. Transformation In Metals And Alloys, Vol. I., Pergamon Press Ltd., Oxford, 1975.

47. C. N. R. Rao and K. J. Rao. Phase Transition In Solids. McGraw-Hill Inc., 1978.

48. S. F. Ahmad. Ph.D. Thesis, Memorial University of Newfoundland, St. John's. 1981.

49. S. F. Ahmad, H. Kiefte, M. J. Clouter and M. D. Whitmore. Phys.

Rev. B, 26, 4239 (1982).

50. B. D. Cullity. X-Ray Diffraction. Addison-Wesley Pub. Co., Inc., Massachusetts, 1967.

51. R. E. Gagnon. Honors Thesis. Memorial University Of Newfoundland, St. John's. 1978.

52. J. P. Frank and W. B. Daniels. Phys. Rev. B, 24, 2456 (1981).

53. R. L. Mills, J. L. Yarnell and A. F. Schuch in reference (66), P. 426.

54. J. L. Yarnell, R. L. Mills and A. F. Schuch in reference (66), P. 426.

55. R. W. Impey and M. L. Klein. Chem. Phys. Let. 104, 579 (1984)

56. P. A. Bezuglyi. L. M. Taransenko and Yu. S. Ivanov. Sov. Phys. Sol. St. 10, 1660 (1969).

57. D. T. Cromer, R. L. Mills, D. Schiferl and L. A. Schwalbe. Acta Cryst. B, 37, 8 (1981).

58. C. Laird and H. I. Aaronson. Acta Meta. 15, 73 (1967).

59. P. S. Kotval and R. W. K. Honeycombe. Acta Meta. 16, 597 (1968).

60. J. W. Christian. Proc. R. Soc. Lon. A, 206, 51 (1951).

61. H. Shoji. Z. Kryst. 77, 381 (1931).

62. J. P. Franck. Chem. Phys. Let. 63, 100 (1979).

63. J. P. Franck. Phys. Rev. B, 22, 4315 (1980).

64. A. F. Schuch, R. L. Mills and D. A. Depatie. Phys. Rev. 165, 1032 (1968).

65. W. N. Hardy, I. F. Silvera and J. P. McTague. Phys. Rev. Let. 26, 127 (1971).

66. I. F. Silvera. Rev. Mod. Phys. 52, 393 (1980).

67. G. C. Defotis. J. Chem. Phys. 71, 5336 (1979).